A Sensitive Temperature Sensor with a Large Dynamic Spectral Range Based on a Dual-emissive Thermally Activated Delayed Fluorescence Dendrimer System

Changfeng Si,[a] Dianming Sun,[a] Eli Zysman-Colman[a]**

[a] Organic Semiconductor Centre, EaStCHEM School of Chemistry, University of St Andrews, St Andrews, Fife, UK. KY16 9ST, Fax: +44-1334 463808; Tel: +44-1334 463826

Corresponding: eli.zysman-colman@st-andrews.ac.uk

Key words: thermally activated delayed fluorescence, dendrimers, dual emission, aggregates, temperature sensor, solution-processed OLEDs

Abstract

Dual emission from organic thermally activated delayed fluorescence (TADF) emitters is often difficult to observe, especially in the solution-state, because most compounds adhere to Kasha's rule where emission originates from the lowest energy excited state. Two TADF dendrimers with different rigid and planar N-doped polycyclic aromatic hydrocarbons (PAH) as acceptors were designed and synthesized. By modulating the molecular geometry, compound **2GCzBPN** that possesses a strongly twisted geometry exhibits TADF, while **2GCzBPPZ**, possessing a less twisted geometry, shows dual emission with an emission peak at 475 nm associated with the monomer and one at 575 nm linked to aggregates that is TADF. This dual emission is both concentration-dependent and temperature-dependent in solution. This is the first observation of aggregate emission from TADF dendrimers in solution. The control of the contributions from intramolecular and intermolecular charge-transfer states permits a wide color tuning from sky blue through white to yellow light emission. We demonstrate how **2GCzBPPZ** can serve as a temperature sensor and exhibits excellent temperature sensitivity across a very wide temperature range (−70 °C to 70 °C) in *n*-hexane, accompanied by a significant spectral response, ranging from yellow to white, and then blue emission, which is the widest detected temperature range and color response reported for an organic luminescent material in solution and also to the best of our knowledge the first small molecule TADF compound used for colorimetric temperature sensing. By embedding **2GCzBPPZ** into paraffin, we demonstrated a spatio-temperature sensor that showed a noticeable emission shift from yellow to green and ultimately to blue as the temperature increased from 20 °C to 200 °C. Finally, solution-processed organic light-emitting diodes (OLEDs) using these two dendrimer emitters showed divergent performance, with a three-times higher maximum external quantum efficiency

(EQE_{max}) of 15.0% for the device with **2GCzBPPZ** compared to the device with **2GCzBPN** (5.3%).

Introduction

Thermally activated delayed fluorescence (TADF) materials have attracted much attention in the last decades as replacement emitter materials for noble-metal based phosphorescent complexes in OLEDs, due to their comparable ability to harvest up to 100% of the triplet excitons to produce light, while simultaneously being less expensive and using more sustainable elements.[1–3] TADF relies on there being a relatively small energy gap (ΔE_{ST}) between the lowest energy triplet state (T_1) and the lowest energy singlet state (S_1) to enable reverse intersystem crossing (RISC) at ambient temperatures. To obtain a small ΔE_{ST} in purely organic molecules, the most widely adopted strategy is to introduce a strongly twisted donor-acceptor (D-A) system, that produces an S_1 state of intramolecular charge transfer character, and which also results in a compound where there is a small overlap of the electron density between the highest occupied molecular orbital (HOMO) and the lowest unoccupied molecular orbital (LUMO).[2,4] Most of the TADF, and indeed most emissive, compounds only emit from a single, low-lying excited state, adhering to Kasha's rule.[5,6]

Several strategies have been advanced to design organic TADF molecules that show dual-emission characteristics from a single component, behavior that could be exploited to produce white-light emission,[7] or in sensing[8] or bioimaging.[9] Dual emission can be induced where an emissive compound exists in multiple conformations, each with their distinct photophysical properties. First reported by Adachi and co-workers, who designed a D-A TADF emitter, **PTZ-TRZ** (Figure **1**), this compound exists in both a quasi-axial (A) and quasi-equatorial (E) conformation and shows dual ICT fluorescence.[10] Li *et al.* reported the compound **a-DMAc-TRZ**, which shows emission from two different conformations.[11] Dual emission can also arise from equilibrated LE and CT excited states.[12] Geng *et al.* designed two molecules, **TMCz-σ-TRZ** and **DMAC-σ-TRZ**, that contain a hexafluoroisopropylidene σ- bridging unit between the D and A moieties. Both of these D-σ-A compounds showed simultaneous emission from LE and CT states, the latter of which showed TADF character.[13] Another design involves the dual emission from hybrid intramolecular and intermolecular CT excited states. Most TADF systems emit from either an intramolecular CT (intra-CT) excited state or an intermolecular CT (inter-CT) excited state, such as exists in an exciplex; however, there are a limited number of reports of TADF systems where there is a coexistence of intra- and inter-CT states.[14,15] For instance, Chi and co-workers explored four asymmetrical D-A-D' compounds, **CPzP**, **CPzPO**,

SPzP and **SPzPO**, each showing dual emission. In solution, as the concentration increased, the emission maximum of the high-energy intra-CT bands remained unchanged whereas the low-energy inter-CT bands increased in intensity significantly, which the authors attributed to the enhanced C–H···O hydrogen bonding between adjacent molecules.[14] Finally, some TADF molecules containing an asymmetric triad structure showed dual emission emanating from two different ICT transitions from different donors to a common acceptor. For example, Zhu *et al.* developed a TADF emitter that combined PTZ (D) and *N*-(1*H*-indole-5-yl) acetamide (D') as donors each attached to the same diphenylsulfone acceptor that showed dual emission.[9] The formation of an intermolecular H-bonding network and the quasi-equatorial conformation of the PTZ made the dual TADF emission strong both in dilute solution and in the aggregated state.

In addition to the aforementioned strategies, modulating the ratio of excimers/aggregates versus monomer species would be another strategy to obtain dual emission systems.[16–22] Generally, excimer formation is favored when the structure of the emitter is rigid and planar, such as is found in anthracene,[23] pyrene,[24] and fluorene.[25] However, those type of polycyclic aromatic hydrocarbons (units) are not suitable for constructing TADF compounds as their triplet energies are too low in energy, leading invariably to compounds with large ΔE_{ST}, regardless of donor substitution. Excimers are uncommon in highly twisted D-A TADF compounds due to sterics that impede the required intermolecular π-stacking interactions.[26,27] Aggregates are clusters of molecules that are held together by intermolecular interactions and form in the ground state, unlike excimers that form in the excited state.[28–31] However, most emissive aggregates exhibit a single emission band that is red-shifted (J-aggregation) or blue-shifted (H-aggregation) compared to the emission of the monomeric species.[32–34] There are relatively few examples of dual emission TADF systems resulting from a combination of monomer and aggregate emission, especially in the solution state.[35]

Optical temperature sensing using organic fluorophores has been developed over the past two decades, there are now examples of organic temperature sensors that show high sensitivity, fast response, simple operation, and have been used in diverse applications such as bioimaging,[36–41] fluorescent thermometers,[36] and microfluidic.[42] Detection using these sensors typically relies on the temperature dependence of one of the emission intensity,[43] wavelength,[44,45] and lifetime.[46] Most of the small molecule temperature-sensitive fluorescent probes are derived from rhodamine, BODIPY, or molecules emitting from a twisted intramolecular charge transfer (TICT) state, whose emission intensity and/or lifetime are temperature dependent and where

the sensors operate typically over a narrow temperature range from around 20 °C to 70 °C.[37,47–49] Organic TADF materials have also shown promise as temperature sensors.[8,33–39] However, most TADF-based temperature sensors rely only on changes in the emission lifetimes or emission intensity of the materials, which are governed by the endothermic nature of the RISC processes. For example, Farinha and co-workers reported the encapsulation of C_{70} in polymer nanoparticles, this system shows a emission intensity increase with increasing temperature, corresponding to a working range from −75 °C to 105 °C.[54] Borisov and co-workers developed TADF-based temperature probes by encapsulating TADF compounds in a low-oxygen permeability polymer (P(VDC-*co*-AN)), these materials feature good temperature sensitivity in the range of 5°C to 50 °C with 1.4–3.7% K^{-1} change of delayed lifetime, τ_d, at 298 K.[51] However, these two examples of temperature sensors that rely on emission lifetime or intensity change are generally more complex to integrate into devices than traditional temperature sensors due to the need for specialized instrumentation for their excitation and detection, thereby limiting their wider use. A second class of TADF-based temperature sensors rely on changes in emission color; however, there are very few reports of spectral TADF temperature sensors. Hudson and co-workers designed a temperature-responsive polymer by co-polymerization of the TADF monomer, **NAI−DMAC**, with *N*-isopropylacrylamide and a blue, fluorescent dopant (tBuODA) as a Förster resonance energy transfer (FRET) acceptor. The polymer was used as a ratiometric temperature sensors that varied its color from red TADF emission at room temperature to blue fluorescence at 70 °C, showing a high ratiometric fluorescent thermal response of 32 ± 4% K^{-1} over a temperature range from 20 °C to 70 °C.

In this study, two different rigid and planar N-doped PAHs were employed as the acceptors in two TADF dendrimers containing a second-generation tercarbazole donor dendron, 3",6,6"-tetrakis(*tert*-butyl-9 ″ H-9,3":6",9"'-tercarbazole) (GCz). The chemical structures of the dendrimers 12,15-bis(3,3",6,6"-tetra-*tert*-butyl-9'*H*-[9,3':6',9"-tercarbazol]-9'-yl)dibenzo[*a,c*]dipyrido[3,2-*h*:2',3'-] phenazine (**2GCzBPPZ**) and 11,12-bis(3,3",6,6"-tetra-*tert*-butyl-9'*H*-[9,3':6',9"-tercarbazol]-9'-yl)dipyrido[3,2-*a*:2',3'-*c*]phenazine (**2GCzBPN**) are shown in Figure **1e**. Compound **2GCzBPPZ** possesses a complex concentration- and temperature-dependent dual emission where the longer wavelength emission band shows TADF. Through a combination of detailed photophysical studies and theoretical calculations we attribute to the emission from both monomolecular and aggregates species. Due to the more twisted geometry and the presence of bulky substituents, **2GCzBPN** exhibits TADF and aggregates formation is suppressed. The distinct photophysical properties of **2GCzBPPZ** motivated us to use it as a temperature sensor. **2GCzBPPZ** exhibits excellent temperature

sensitivity across a very wide temperature range (–70 °C to 70 °C), corresponding to a large color change from yellow at –70 °C through white at room temperature to sky blue at 70 °C, which is to the best of our knowledge one of the best TADF-based temperature sensors based on its large dynamic spectral range and associated wide temperature detection range emanating from a single material. Finally, we also employed these two dendrimers as emitters in solution-processed OLEDs.

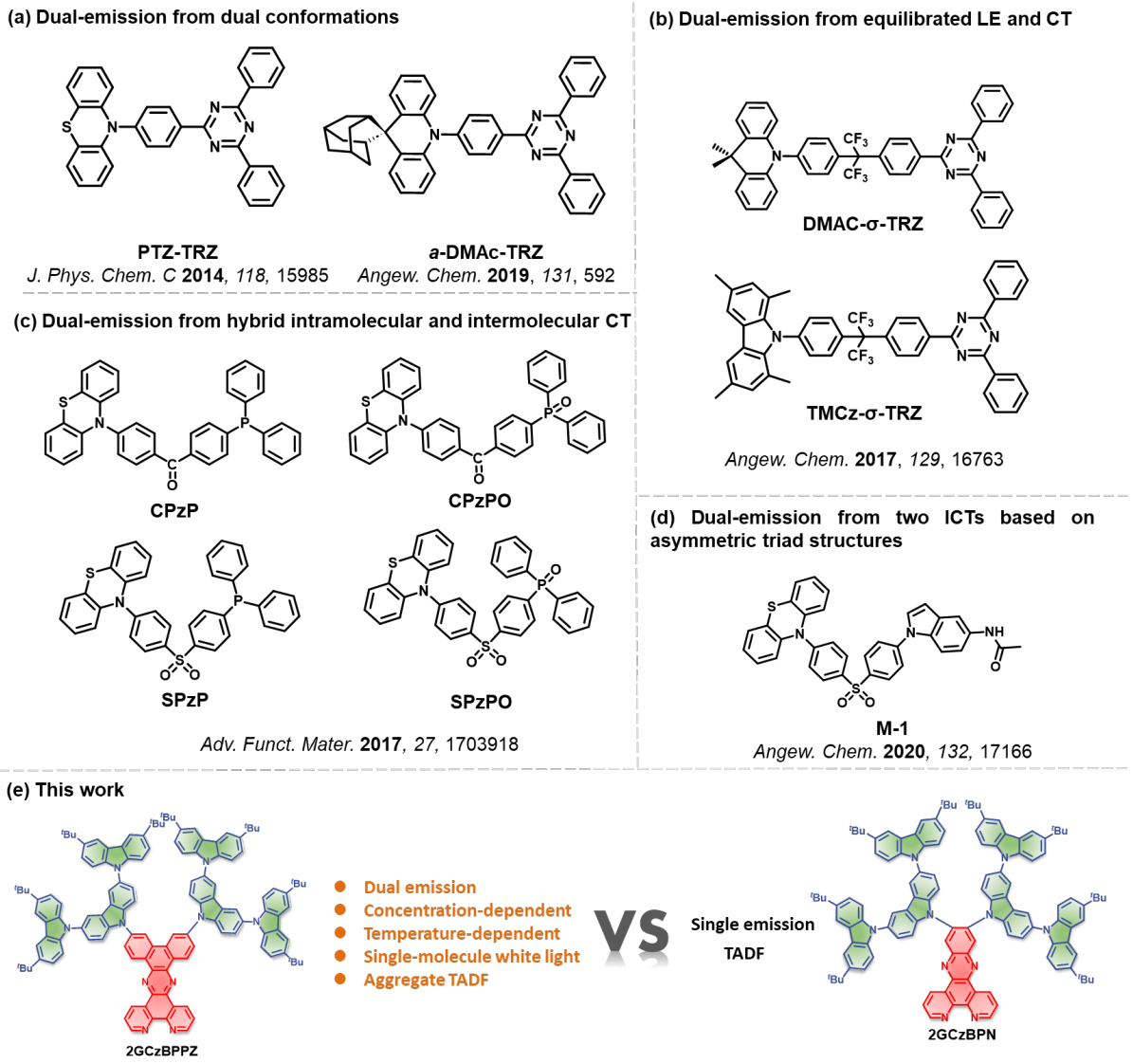

Figure **1**. Dual emission from (a) dual conformations, (b) equilibrated LE and CT states, (c) "hybrid intramolecular and intermolecular CT" states and (d) two ICT states based on asymmetric triad structures; (e) this work: dual emission from TADF monomers and aggregates.

Synthesis

Scheme **S1** shows the synthetic routes for **2GCzBPPZ** and **2GCzBPN**. Intermediates **1** and **2** were synthesized by, respectively, coupling G2Cz to the corresponding halogenated acceptor core via a Buchwald-Hartwig C-N cross-coupling or by nucleophilic aromatic substitution reaction in yields of 80 and 83%. Emitters **2GCzBPPZ** and **2GCzBPN** were obtained by the condensation reaction of **1** and **2** with 1,10-phenanthroline-5,6-diamine and 1,10-phenanthroline-5,6-dione, respectively. The identity and purity of the two emitters were verified by ^{1}H NMR, ^{13}C NMR spectroscopy, melting point determination, high resolution mass spectrometry and elemental analysis and high-performance liquid chromatography (HPLC) (Figures **S1-S16**).

Theoretical Calculations

The ground-state (S_0) geometries of **2GCzBPPZ** and **2GCzBPN** were optimized using density functional theory (DFT) at the PBE0[57]/6-31G(d,p) level[58] of theory in the gas phase starting from a geometry generated using Chem3D.[59] At the optimized S_0 geometries (Figure **S17**), due to the larger steric hindrance caused by two of the 2GCz donors substituted on neighboring positions of the BPN acceptor, **2GCzBPN** possesses a much more twisted geometry than that of **2GCzBPPZ**, where the torsion angles between donor and acceptor were on average about 67° and 43°, respectively. The frontier molecular orbital (FMO) of **2GCzBPPZ** and **2GCzBPN** are shown in Figure **2a** and **S18**. As expected, the highest occupied molecular orbitals (HOMOs) are localized on the donors while lowest unoccupied molecular orbitals (LUMOs) are localized on the acceptor group. Notably, as shown in Figure **S19**, BPPZ (LUMO = –2.19 eV) is a weaker electron-acceptor than BPN (LUMO = –2.38 eV). Thus, the HOMO-LUMO gap, $\Delta E_{HOMO\text{-}LUMO}$, decreases from 2.87 eV for **2GCzBPPZ** to 2.36 eV for **2GCzBPN**. The excited-state properties were calculated using time-dependent density functional theory (TD-DFT) within the Tamm-Dancoff approximation (TDA-DFT) based on the optimized S_0 geometries (Figure **2b** and **2c**, the excited-state properties were also calculated based on optimized S_1 geometries and are shown in Figure **S20**).[60–62] The S_1 energies are 2.54 eV for **2GCzBPPZ** and 1.95 eV for **2GCzBPN**, while the T_1 energies are 2.43 eV to 1.91 eV, respectively, corresponding to ΔE_{ST} values of 0.11 eV for **2GCzBPPZ** and only 0.04 eV for **2GCzBPN**, due to its more twisted conformation. Figure **2c** displays the natural transition orbitals (NTOs) for S_1 and T_1. For both compounds, the hole and electron densities are clearly separated for S_1, indicating charge-transfer (CT) transitions from the ground state. The T_1 state of **2GCzBPN** is also CT in nature while that of **2GCzBPPZ** is better described as one having a mixed locally excited (LE) and CT character (Figure **S18**). Reflecting the somewhat stronger

overlap between the HOMO and LUMO electron densities, the calculated oscillator strength, *f*, for the S_0-S_1 transition in **2GCzBPPZ** (f = 0.13) is larger than in **2GCzBPN** (f = 0.06). To evaluate the geometric rigidity of the compounds, we calculated the root-mean-square displacement (RMSD) value (Figure **2d**) using the VMD program[63] between S_0 and S_1 geometries each optimized at the PBE0/6-31G(d,p) level. **2GCzBPN** shows a relatively smaller geometry relaxation (RMSD = 0.22 Å) compared to **2GCzBPPZ** (RMSD = 0.41 Å), suggesting that **2GCzBPN** possess a more rigid geometry, so nonradiative decay should be relatively attenuated for this compound compared to **2GCzBPPZ**.

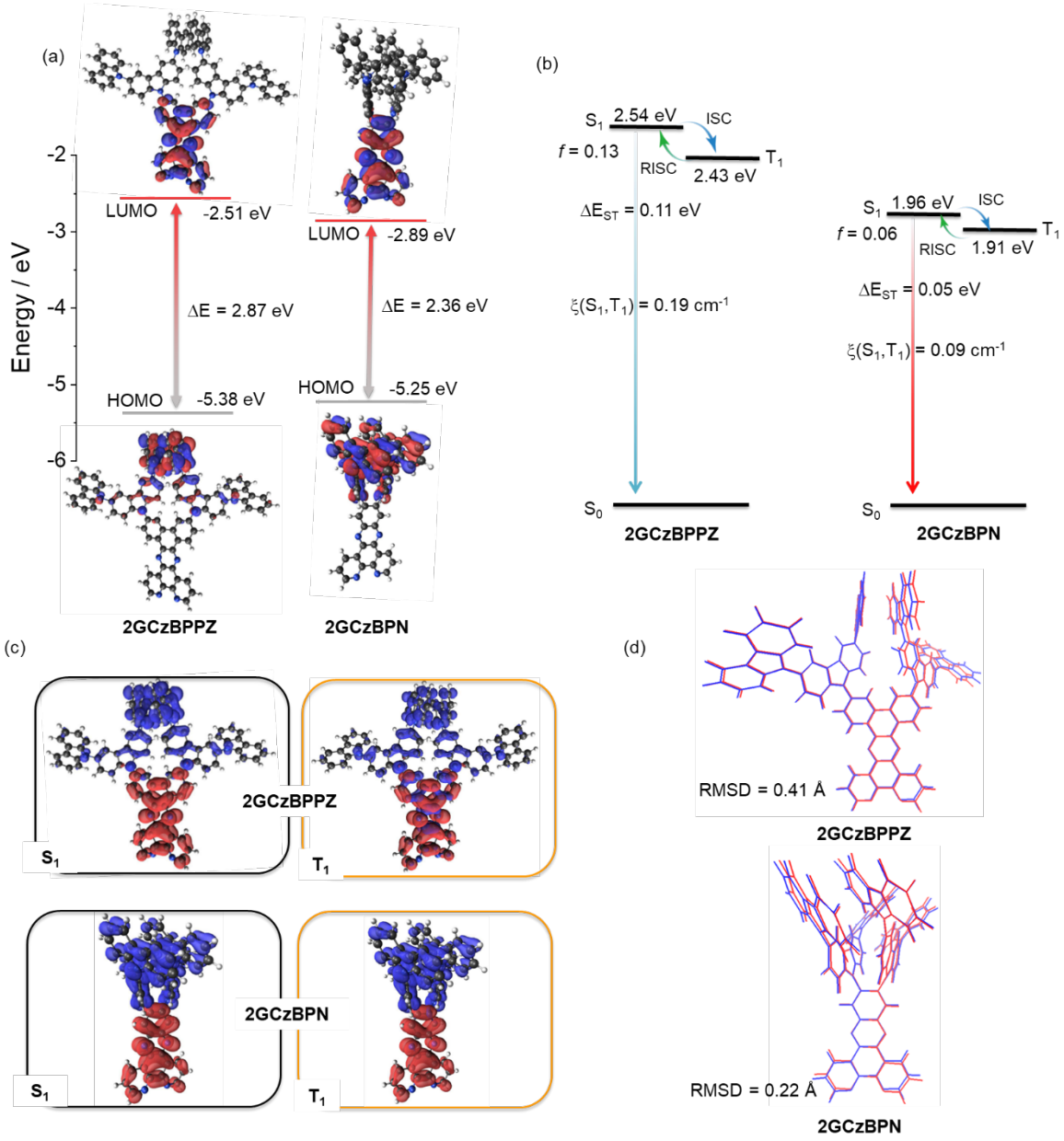

Figure **2**. (a) Frontier molecular orbitals (isovalue: 0.02) and (b) vertical excitation energy levels of **2GCzBPPZ** and **2GCzBPN**, (c) Natural transition orbitals (unoccupied (hole, blue) & occupied (electron, red), (isovalue: 0.02) of S_1 and T_1 for **2GCzBPPZ** and **2GCzBPN**

calculated at the optimized S_0 geometry in the gas phase at the PBE0/6-31G(d,p) level. (d) comparison of optimized structures of **2GCzBPPZ** and **2GCzBPN** at S_0 (blue) and S_1 (red) state.

Electrochemistry

Next, the energies of the frontier molecular orbitals (FMOs) were inferred from the electrochemical behavior of **2GCzBPPZ** and **2GCzBPN** by cyclic voltammetry (CV) and differential pulse voltammetry (DPV) in degassed dichloromethane (DCM) with tetra-*n*-butylammonium hexafluorophosphate ($[^nBu_4N]PF_6$) as the supporting electrolyte (Figure **3a**). The reduction potential (E_{red}), determined from the DPV peak values, are −1.36 V for **2GCzBPPZ** and −1.13 V for **2GCzBPN**, respectively. The inferred LUMO energies of –2.94 eV and −3.21 eV for **2GCzBPPZ** and **2GCzBPN**, respectively, are consistent with the trend of the energies from the theoretical calculation (Figure **2a**). **2GCzBPPZ** and **2GCzBPN** both have two resolvable quasi-reversible oxidation waves with E_{ox} of 1.00 V and 1.13 V for **2GCzBPPZ**, 0.92 V and 1.07 V for **2GCzBPN**, which correspond to the oxidation of the inner carbazole and the peripheral *tert*-butylcarbazole, respectively.[64,65] Due to the presence of two adjacent donors, **2GCzBPN** has a catholically shifted first oxidation potential (E_{ox} = 0.92 V) than that of **2GCzBPPZ** (E_{ox} = 1.00 V), corresponding to HOMO levels of −5.22 and −5.30 eV, respectively. The HOMO–LUMO gaps are 2.36 and 2.01 eV for **2GCzBPPZ** and **2GCzBPN**, respectively, which mirror the trend in the DFT calculated values of 2.87 and 2.36 eV (Figure **2a**).

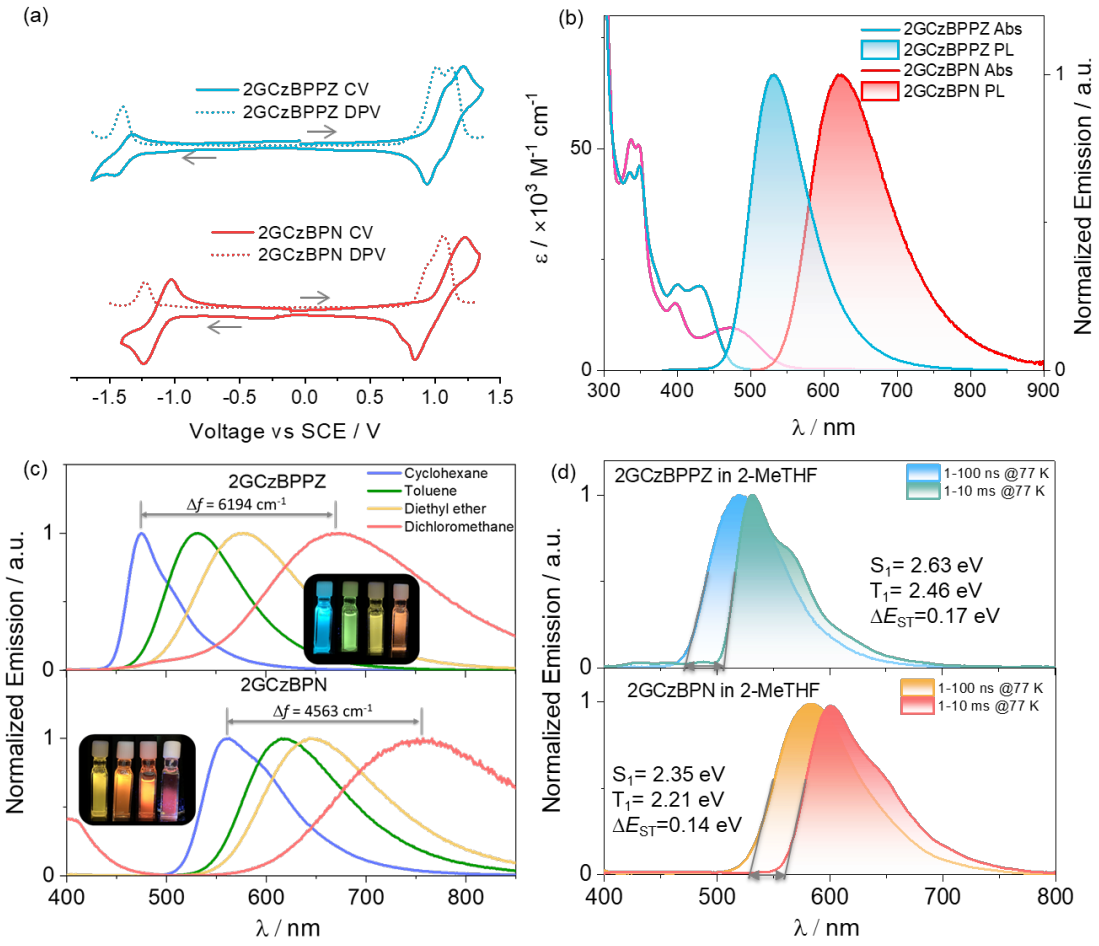

Figure **3**. (a) Cyclic and differential pulse voltammograms measured in degassed DCM with 0.1 M [^{n}Bu$_4$N]PF$_6$ as the supporting electrolyte and Fc/Fc$^+$ as the internal reference (0.46 V vs SCE).[66] Scan rate = 100 mV s^{-1}. (b) UV-vis absorption and steady-state photoluminescence (PL) spectra of **2GCzBPPZ** and **2GCzBPN** recorded in toluene at room temperature (λ_{exc} = 340 nm). (c) PL solvatochromism study of **2GCzBPPZ** and **2GCzBPN** (λ_{exc} = 343 nm). (d) Prompt fluorescence and phosphorescence spectra of **2GCzBPPZ** and **2GCzBPN** 2-MeTHF at 77 K (λ_{exc} = 360 nm, prompt fluorescence and phosphorescence spectra were acquired across a 1-100 ns and 1–10 ms time range, respectively).

Photophysical Properties

The UV-Vis absorption spectra of **2GCzBPPZ** and **2GCzBPN** in dilute toluene are shown in Error! Reference source not found.**b** and **S21**, and the photophysical properties are summarized in Table . Both compounds exhibit similar strong double hump absorption with peaks at 337 and 346 nm, which can be attributed to locally excited (LE) transitions of the 2GCz donors based on a comparison with literature data of 2GCz.[65,67] The absorption band at around 400 nm

for both compounds is assigned to an LE transition of the acceptor moieties as these align with the absorption of BPN (Figure **S22a**).[68] **2GCzBPPZ** possesses a stronger ICT absorption band peaking at 432 nm ($\varepsilon = 19\times10^3$ M^{-1} cm^{-1}) than that of **2GCzBPN** (475 nm, $\varepsilon = 10\times10^3$ M^{-1} cm^{-1}), which is consistent with the calculated higher $f = 0.13$ for **2GCzBPPZ** ($S_0 \rightarrow S_1$) than $f = 0.06$ for **2GCzBPN** ($S_0 \rightarrow S_1$) (Figures **S21**). The unstructured and broad PL spectra in toluene for both compounds indicate excited states with strong ICT character, with peak maxima, λ_{PL}, at 534 nm and 624 nm for **2GCzBPPZ** and **2GCzBPN**, respectively (Error! Reference source not found.**a**). A strong positive solvatochromism is observed for both compounds (Error! Reference source not found.), which is consistent with the CT nature of the emissive excited state. Furthermore, **2GCzBPPZ** exhibits a more significant positive solvatochromism with a $\Delta f = 6194$ cm^{-1} than that of **2GCzBPN** ($\Delta f = 4563$ cm^{-1}), corresponding to the larger transition dipole moment in the excited state, which is corroborated by DFT calculations, for **2GCzBPPZ** (3.63 D) than **2GCzBPN** (2.83 D). The optical bandgaps, E_g, calculated from the intersection of the normalized absorption and emission spectra (Figures **S22b**), are 2.62 eV and 2.26 eV for **2GCzBPPZ** and **2GCzBPN**, respectively. The prompt fluorescence and phosphorescence spectra in 2-MeTHF glass at 77 K were used to extract the S_1 and T_1 energies from their respective onsets (Error! Reference source not found.**3d,** Table). The S_1 energies of **2GCzBPPZ** and **2GCzBPN** are 2.63 and 2.35 eV, and the T_1 energies are 2.46 eV and 2.21 eV, respectively. The corresponding ΔE_{ST} values for **2GCzBPPZ** and **2GCzBPN** are 0.17 eV and 0.14 eV, respectively, which align with the TDA-DFT calculated results (Figure **2b**). The structured character of the phosphorescence spectrum for both emitters implies a T_1 state with LE character, corroborated by the TDA-DFT calculations to mixed ^{3}CT/^{3}LE state (LE localized on the acceptor, especially for BPPZ, Figure **2c**). Time-resolved PL (TRPL) decays of **2GCzBPPZ** and **2GCzBPN** in degassed toluene measured using time-correlated single-photon counting (TCSPC, Figure **S23**) show biexponential kinetics with a prompt fluorescence lifetime, τ_p, of 24.3 ns and a delayed fluorescence lifetime, τ_d, of 7.5 μs, in **2GCzBPN** (Figure **S23**). However, the emission of **2GCzBPPZ** decays monoexponentially with τ_P of 22.3 ns, and no delayed emission is observed. In both compounds, the emission intensity in the toluene solutions was enhanced upon oxygen removal, demonstrating that oxygen is quenching accessible triplet states in both compounds.

Aggregate modulation

Due to the large degree of π-conjugation inherent in both acceptors, there is likely to be strong intermolecular π–π interactions leading to aggregates. To explore and modulate the emergence of emission from the **2GCzBPPZ** and **2GCzBPN** aggregates, we measured the PL spectra of different concentrations of **2GCzBPPZ** and **2GCzBPN** in *n*-hexane solution (Figure **4** and **S24**). As shown in Figure **4a**, there are two emission peaks observed for **2GCzBPPZ** where the high-energy emission band at 475 nm converts to the low-energy emission band at 575 nm as a function of increasing concentration of the emitter, indicating that a new species, either aggregate or excimer, is responsible for the low-energy emission; however, there is negligible change in the emission spectra of **2GCzBPN** with increasing concentration (Figure **S23**). The corresponding emission color of **2GCzBPPZ** evolves from sky-blue to white and then to yellow (Figure **4e**). The corresponding ratios of the intensity of the emission at 475 to 575 nm (I_{475}/ I_{575}) and (I_{575}/ I_{475}) upon increasing concentration are shown in Figure **4b**. An isosbestic point was identified at a concentration of 1.6×10^{-5} M where the emission intensity of the monomer (λ_{PL}= 475 nm) is equal to that of the aggregates (λ_{PL}= 575 nm). Specifically, at low concentrations of **2GCzBPPZ** (<1.6×10^{-5} M), the system is dominated by emission from the monomer as molecules are on average not sufficiently close to each other to form aggregates to any major extent (Figure **4c**). As the concentration increases (>1.6×10^{-5} M), the probability of intermolecular interactions increases, and the population of aggregates begins to grow (Figure **4c**). Figure **4d** reveals that with increasing concentration, the absorption maximum associated with the ICT band of **2GCzBPPZ** monomer at ~432 nm gradually decreases along with the emergence of a red-shifted absorption tail from 452 nm to 550 nm, indicating the formation of aggregates through strong intermolecular interactions in the ground state.[69] [14] Furthermore, the absorption of **2GCzBPPZ** in different solvents at the same concentration also demonstrates that the formation of aggregates occurs in *n*-hexane but not in higher polarity solvents like toluene, diethyl ether, or dichloromethane (Figure **S25**). This is likely due to strong solute-solvent interactions that competitively act to suppress the intermolecular interactions between **2GCzBPPZ** molecules responsible for aggregate formation.[70,71]

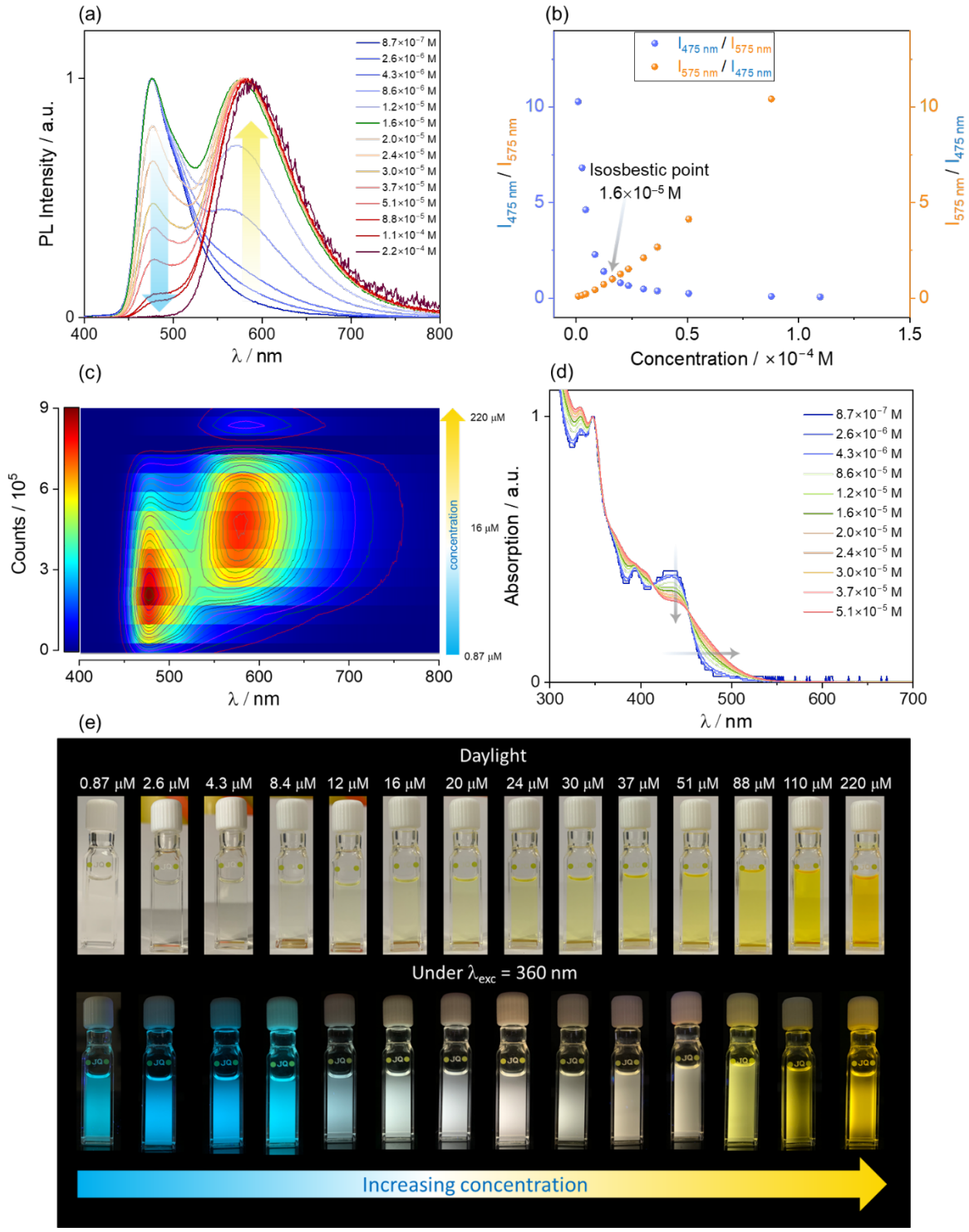

Figure **4.** (a) Concentration-dependent fluorescence spectra for **2GCzBPPZ** in *n*-hexane solution (λ_{exc} = 340 nm); (b) Ratiometric plot of I_{475}/I_{575} (blue dots) and I_{575}/I_{475} (orange dots) vs increasing concentration of **2GCzBPPZ**; (c) Concentration-dependent emission mapping; (d) Concentration-dependent absorption spectra for **2GCzBPPZ** in *n*-hexane solution; (e) Corresponding photos under ambient light and using a UV torch (λ_{exc} = 360 nm);

Figure ***5a*** shows that white emission can be obtained in 2×10^{-5} M solutions of **2GCzBPPZ** in *n*-hexane as a result of contributions from two distinct emission bands at λ_{PL} of 475 and 575 nm. Both emission bands are quenched upon exposure to oxygen, indicating that triplet states are accessible in both emission processes. TRPL studies in *n*-hexane under degassed and aerated conditions reveal that the emission band at 475 nm decays with a similar lifetime, τ_p, of around 5.7 ns (

Figure ***5b*** top), which may reflect the quenching of this emission due to fast Förster resonance energy transfer from the monomers to aggregates (Figure **S26**). Under degassed conditions, the emission band at 575 nm decays with biexponential kinetics, with τ_p of 24.3 ns and τ_d of 7.5 μs, (

Figure ***5b*** bottom), the delayed emission was largely quenched after exposure to air, which could be explained as the quenching of the aggregates-induced TADF in solution.[16,72] We next investigated the photophysical properties of **2GCzBPPZ** as doped films in polymethyl methacrylate (PMMA) (

Figure ***5c***). For the 0.1 wt% doped film in PMMA, **2GCzBPPZ** exhibits a weak green emission with the main peak at 515 nm and shoulder peak at 580 nm. With increasing doping concentration, the intensity of the high-energy emission band decreases while the low-energy emission band becomes dominant, reflecting a similar behavior to that observed in *n*-hexane solution. The TRPL decays reveal biexponential decay kinetics with associated τ_p and τ_d for both emission bands in 0.1 wt% doped film in PMMA. The delayed lifetime of the low-energy emission band decreased from 2.12 ms to 150.5 μs with increasing doping concertation from 0.1 wt% to 50 wt% (Figure **5d**). While the corresponding prompt lifetime slightly increased from 18.7 ns to 25.9 ns with increasing doping concertation.

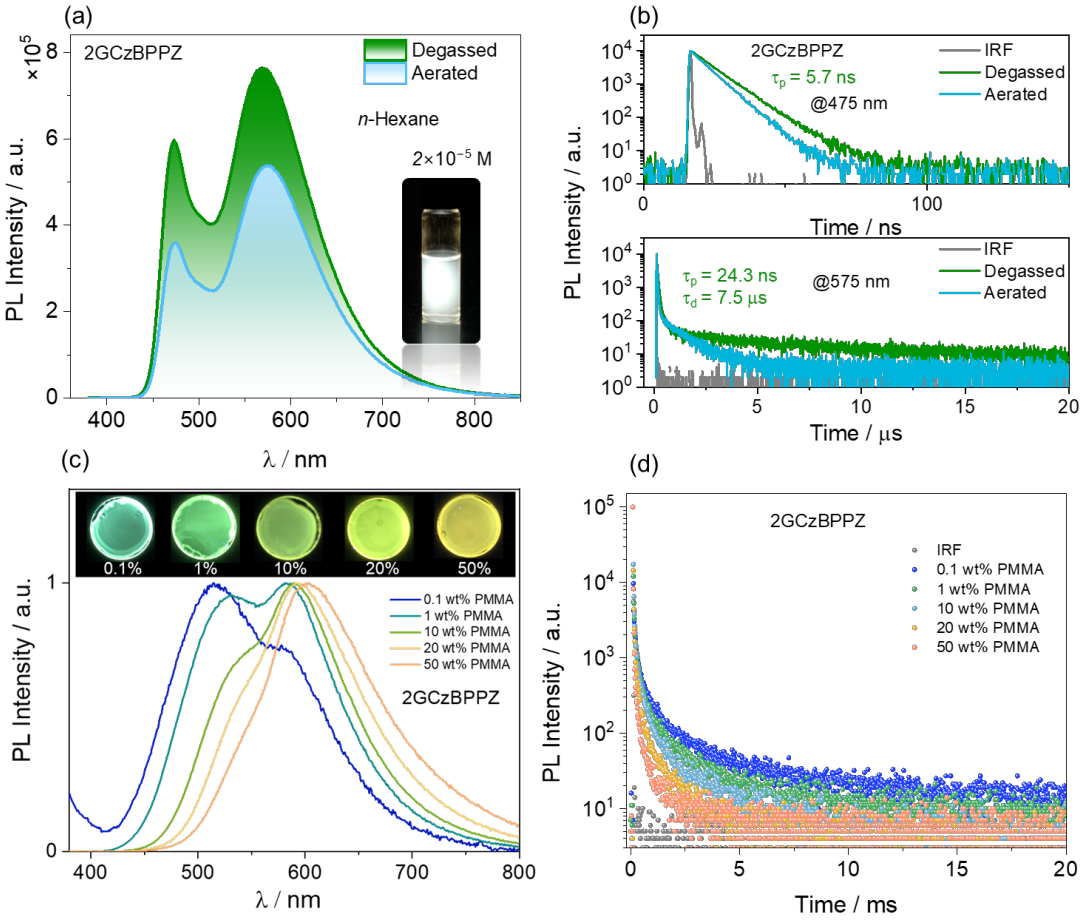

Figure **5.** (a) PL spectra under degassed and aerated conditions at the concentration of 2.0×10^{-5} M in *n*-hexane (λ_{exc} = 340 nm); (b) PL decay of the emission λ_{em}= 475 nm (top) and λ_{em} = 575 nm (bottom) under degassed and aerated *n*-hexane (λ_{exc} = 375 nm); (c) Normalized fluorescence spectra of increasing doping concentrations (from 0.1 wt% to 50 wt%) for **2GCzBPPZ** in PMMA (λ_{exc} = 340 nm); (d) the corresponding PL decays of the doped films in PMMA (λ_{exc} = 340 nm).

Colorimetric temperature sensing

*Intrigued by the unusual dual-emissive nature of **2GCzBPPZ**, we sought to explore in greater detail the photophysical properties and studied the temperature-dependence of the emission in*

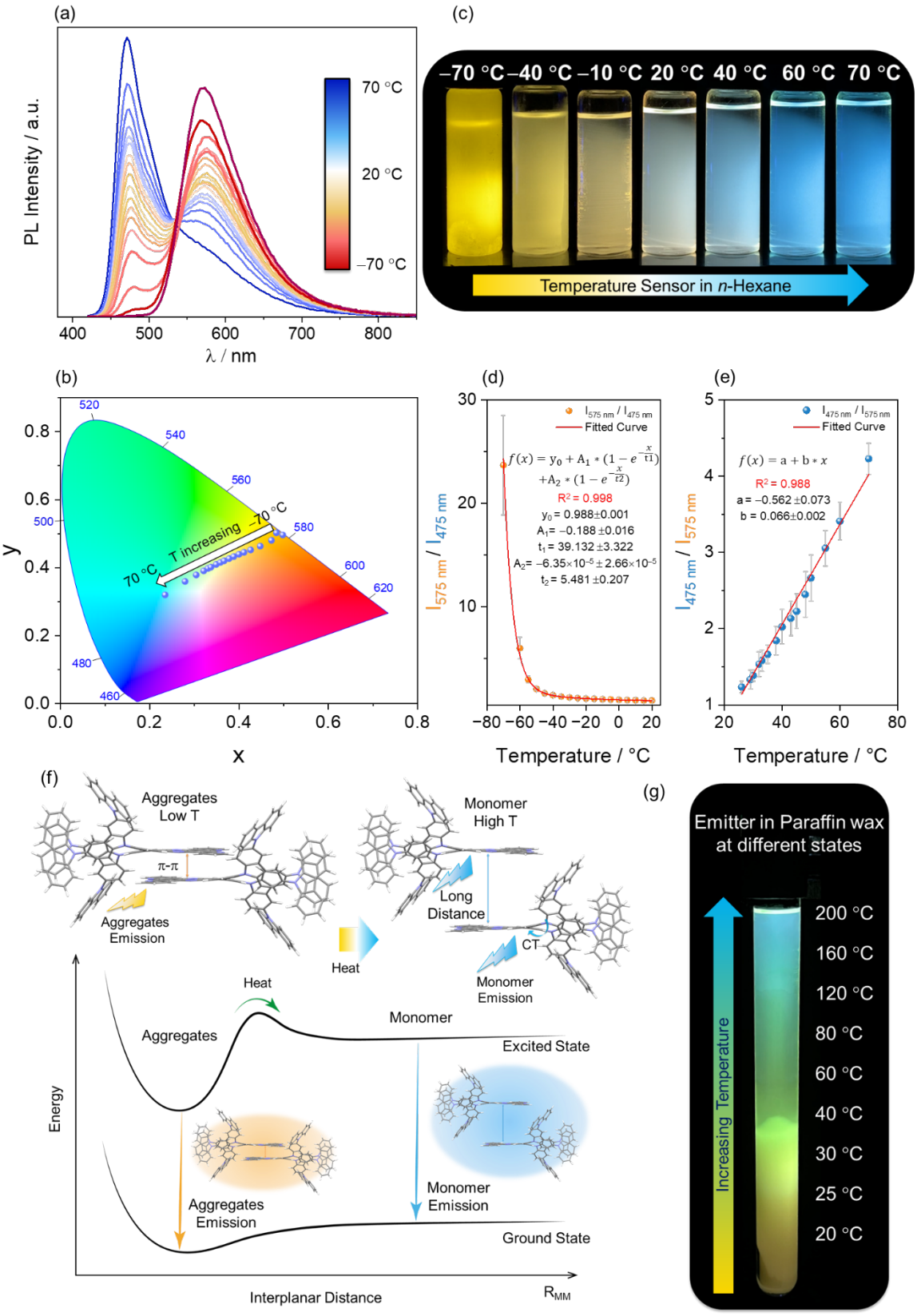

Figure **6**). *At room temperature, the 1.6×10⁻⁵ M solution of* ***2GCzBPPZ*** *is dual-emissive and the sample appears to emit white light (*

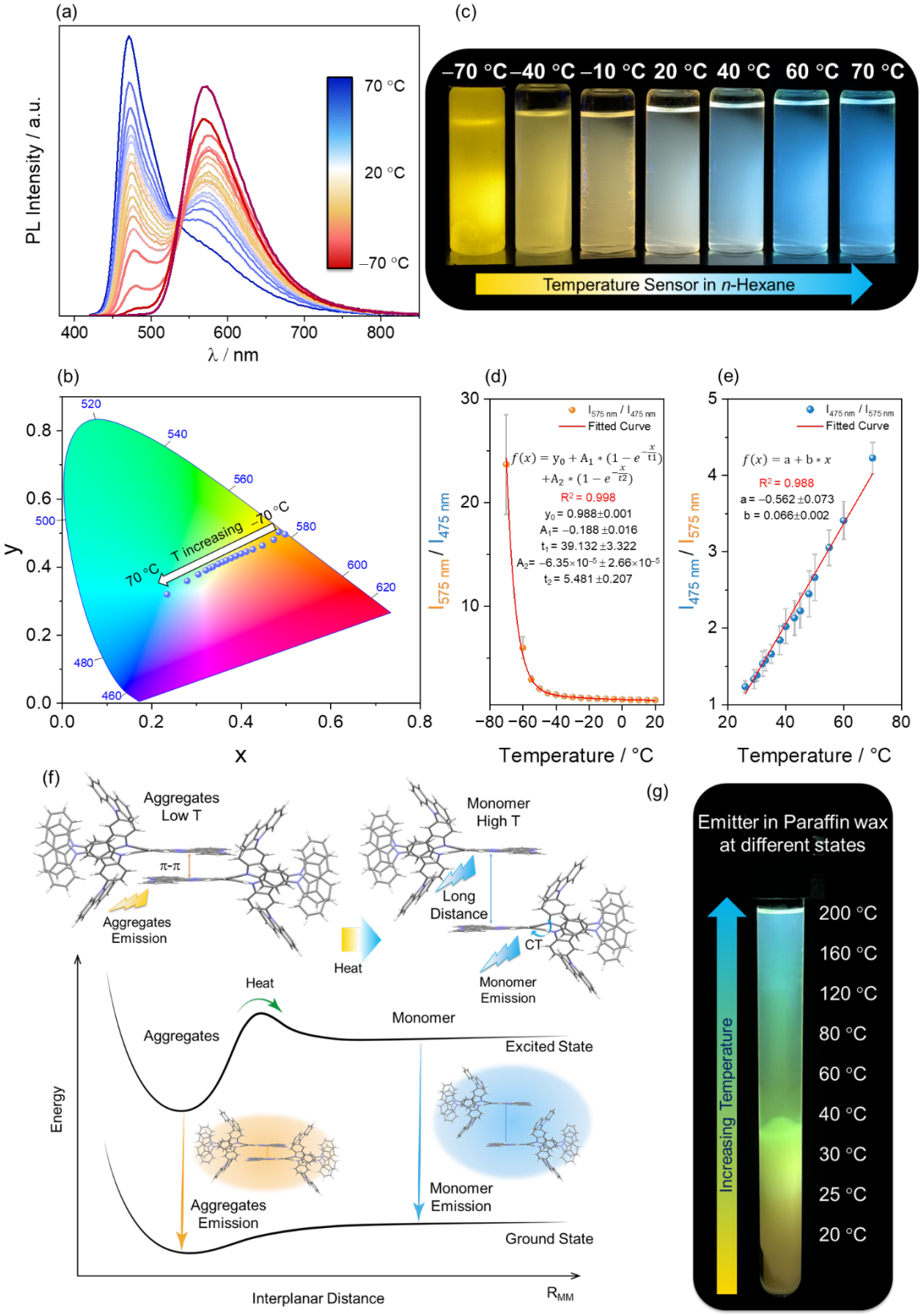

Figure **6*a*** *and* **6*c***), *where there is approximately equal contributions from the emission from the monomer (475 nm) and aggregates (575 nm). Upon decreasing the temperature towards the solvent freezing point, the low-energy emission band increases in intensity dramatically while the high-energy emission band is completely quenched. The corresponding ratio of the intensity of the emission at 575 to 475 nm (I_{575}/I_{475}) exponentially decreases with increasing*

temperature from –70 ° C to room temperature (r^2 = 0.998) (

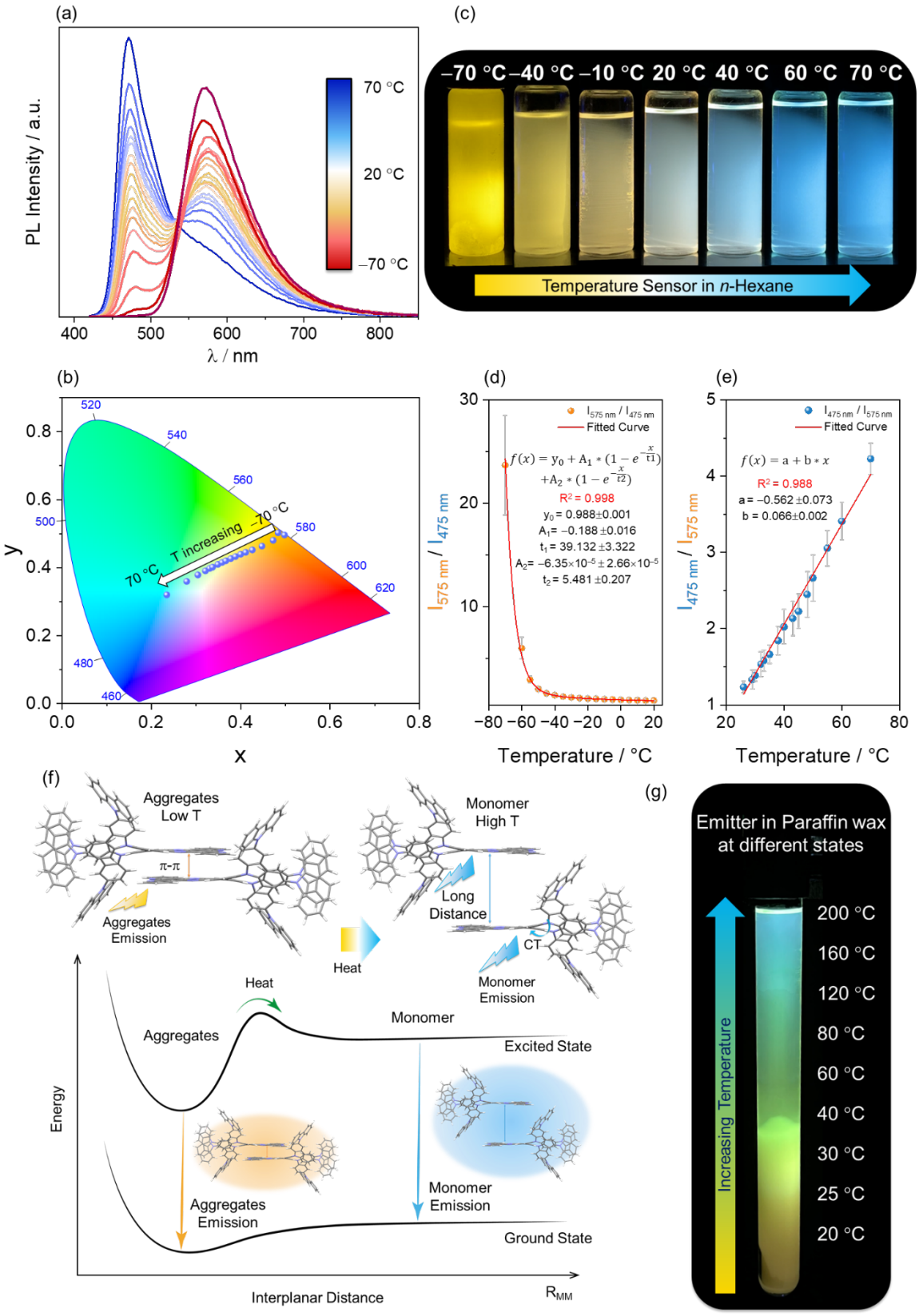

Figure **6***d*). *Such an exponential relationship could result from a combination of various factors at low temperature, like high viscosity and low solubility that will both affect the population of*

the aggregates.[73,74] On the other hand, increasing the temperature beyond room temperature reveals a complementary effect where the high-energy emission band becomes more intense and the low-energy emission band all but disappears. In this temperature regime there is a linear relationship between I_{475}/I_{575} versus T (r^2 = 0.988 over a temperature region of 25 to

70 °C), corresponding to a ratiometric increase of 6.6% ± 0.2% K^{-1} (

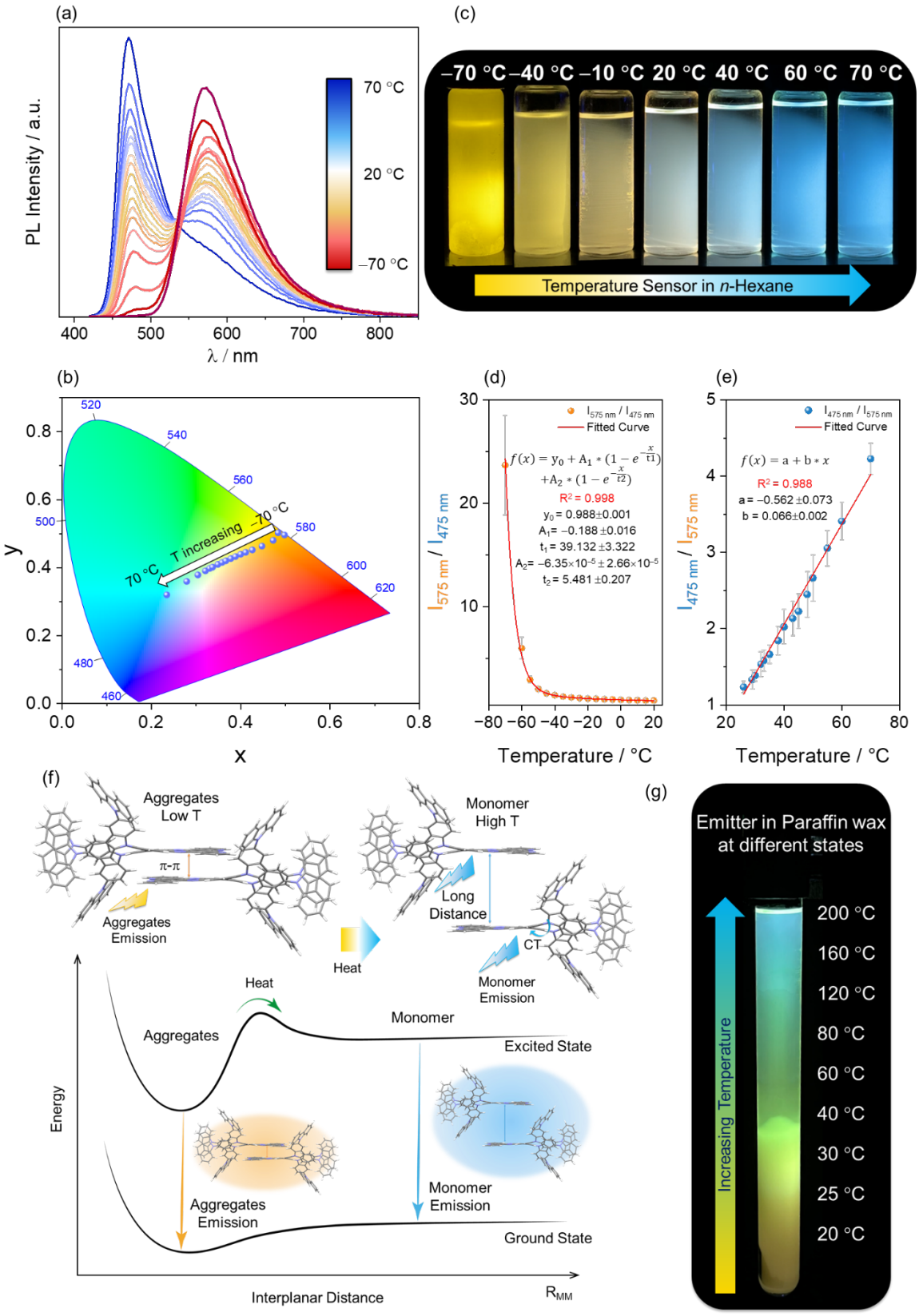

Figure **6***e). Overall,* ***2GCzBPPZ*** *features excellent temperature sensitivity across a broad range of –70 ℃ to 70 °C, manifested in distinct colorimetric readout from yellow at –70 °C to*

white at RT and finally to sky blue at 70 °C, corresponding to CIE coordinates of (0.50, 0.49) at –70 °C that shift to CIE coordinates of (0.23, 0.32) associated with blue emission (

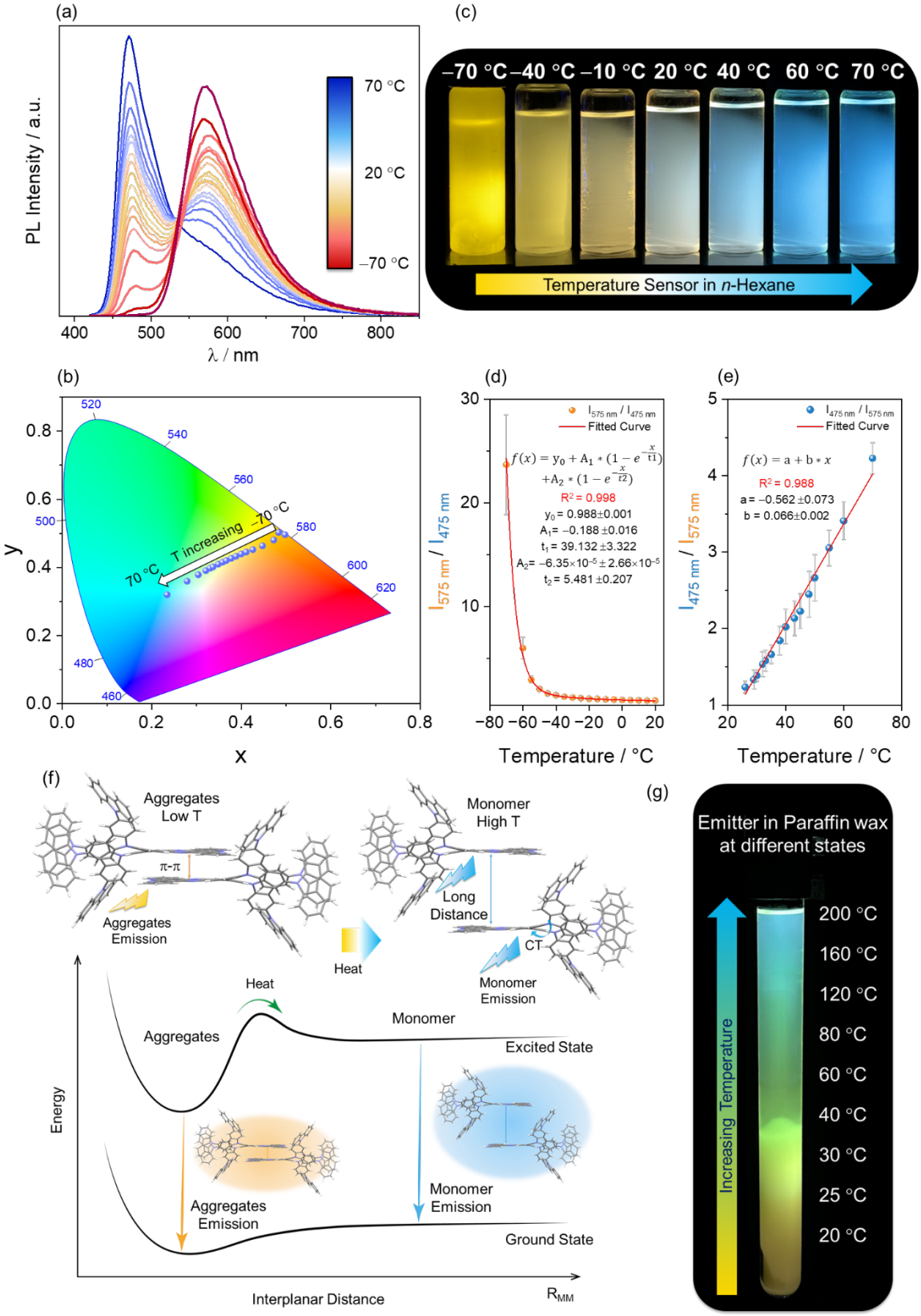

Figure **6*b*** *and ESI Video **1**). The broad range of temperature detection coupled with the significant color change exhibited by **2GCzBPPZ** make it a promising temperature sensor, whose properties are much superior to previously reported organic fluorescent temperature sensors.*[37–39] *Generally, most organic fluorescent temperature sensors rely only on changes in emission intensity with negligible color change and have a narrow temperature detection range, usually of between RT to ~70 °C.*[37–39,47–49] *We have interpreted the origin of the wide dynamic spectral range of our optical temperature sensor to result from a temperature-dependent*

equilibrium between monomeric and aggregate species. Illustrated in

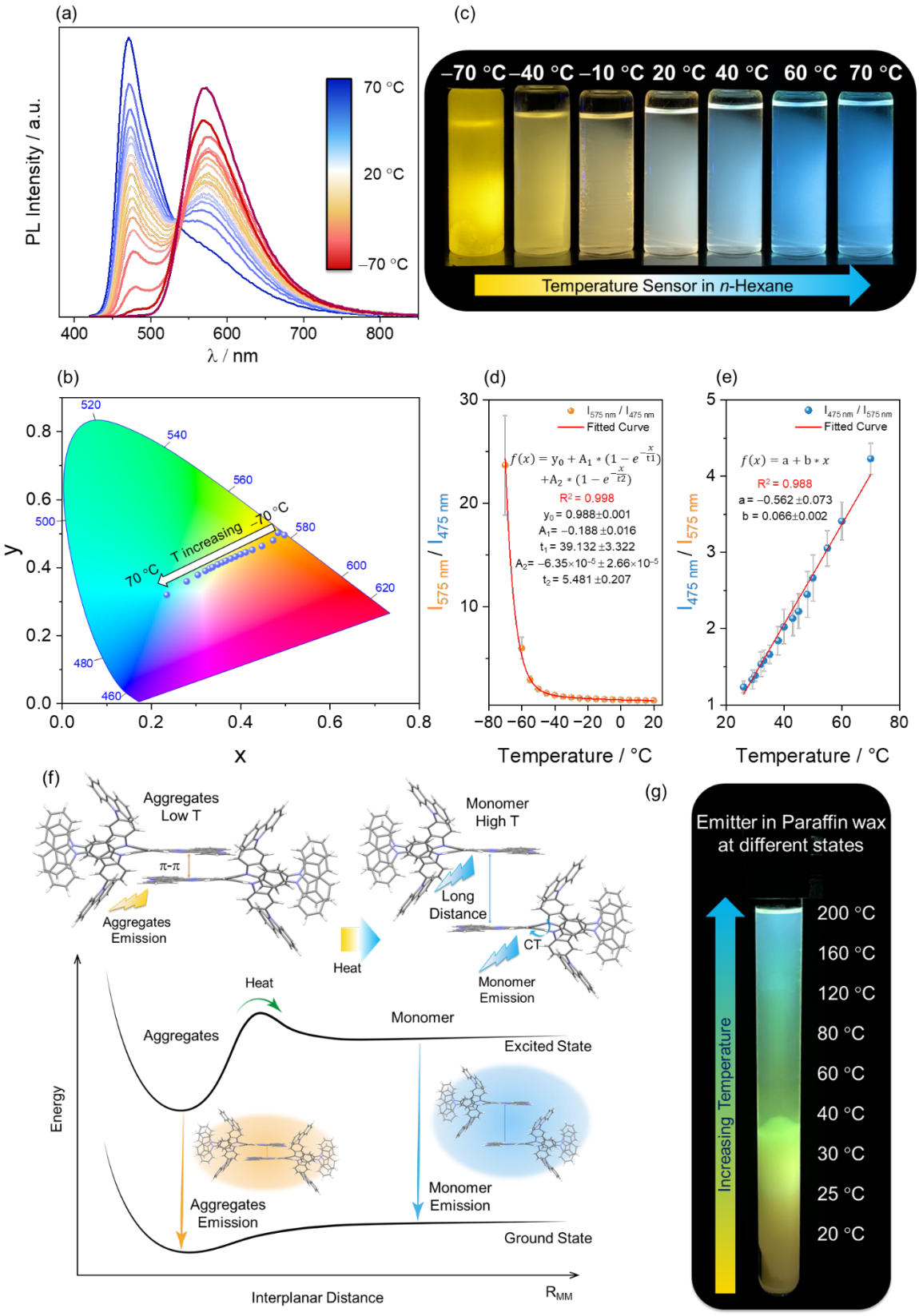

Figure ***6f***, upon increasing the temperature, the π-stacking interactions necessary for aggregate formation are disrupted and the monomer population increases, reflected in the emergence of

blue emission. As the temperature is decreased, the mobility of the molecules in solution is reduced, which can increase the probability of intermolecular interactions and promote the formation of aggregates as the molecules have less energy to overcome the repulsive forces between them and the attractive forces become more significant. Note that FRET occurs from monomer to the aggregates and so as the population of aggregates increases, so does the FRET rate, leading to an accelerated quenching of the high-energy emission of the monomeric species.

Recognizing the potential of this compound to act as a temperature sensor, we translated its properties into the solid state by embedding the compound into Paraffin. As shown in Figure **6g**, when photoexcited at 360 nm the solid Paraffin emits in the yellow at room temperature. As the temperature increases from 20 towards 80 °C, paraffin starts to melt at around 50 °C and the emission gradually blue-shifts from yellow to green. When the temperature increases beyond 160 °C, the liquid paraffin emits in the blue, emulating the emission observed in *n*-hexane beyond 60 °C. This distinctive performance in paraffin makes it ideal as a spatio-temperature probe. As demonstrated in Figure **6g** and ESI Video **2** in the ESI, the **2GCzBPPZ**-embedded paraffin was melted and poured into a test tube (length:160 mm, diameter: 16 mm) and then allowed to solidify upon cooling. At room temperature, the entire test tube with the solid paraffin shows yellow emission. As the top part of the temperature is selectively heated and the local temperature increases, this part of the paraffin sample exhibits a noticeable color change, while the bottom section of the paraffin maintains its yellow emission as this part is still at room temperature. We have correlated the optical response of the **2GCzBPPZ**-embedded paraffin with an external temperature probe to demonstrate that it can act as an accurate temperature sensor (Figure **S27**, see also ESI Video **3** in ESI). In an attempt to use a non-polar solid host with a higher melting temperature, we also incorporated **2GCzBPPZ** into 4,4'-bis(9-carbazolyl)-biphenyl (CBP). However, despite having a similar polarity to paraffin, dual emission was not observed in this host. Although the doped film of **2GCzBPPZ** in PMMA exhibits concentration-dependent dual emission (

Figure ***5c***) there was no temperature-dependent emission observed, which implies that in this host it is not possible to change significantly intramolecular distances as a function of temperature. The fact that the optical thermometer phenomenon works in paraffin but not the other hosts may be due to the paraffin having a greater thermal expansion coefficient compared to these other host compounds.[75] **2GCzBPPZ** thus shows unrivaled temperature sensitivity and with a broad temperature-dependent spectral response compared to previously reported organic temperature sensors.[36–41]

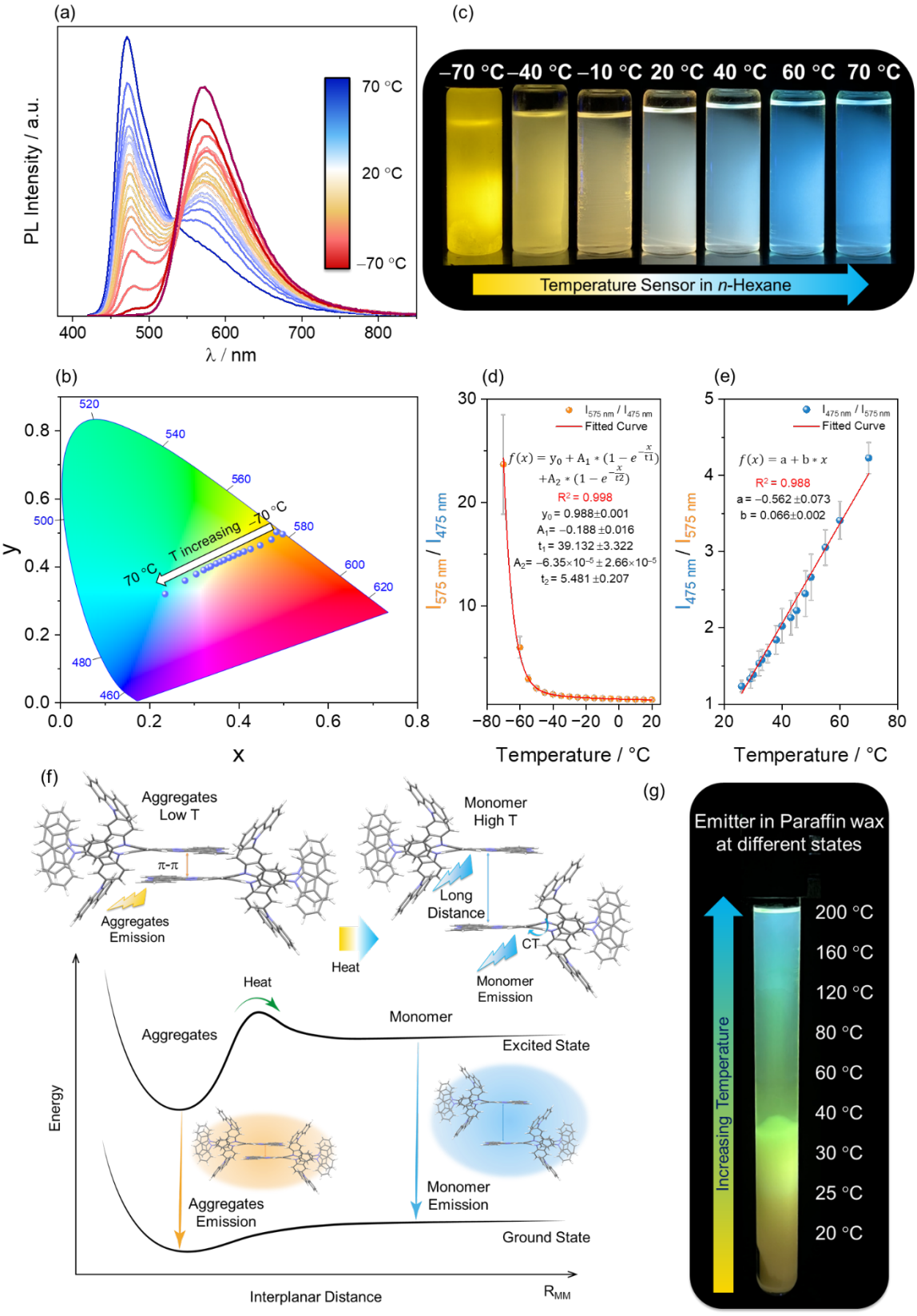

Figure **6**. (a) Temperature-dependent emission spectra of **2GCzBPPZ** in *n*-hexane at a concentration of 1.6×10^{-5} M (λ_{exc} = 360 nm); (b) CIE plot of the emission spectra in (a) of **2GCzBPPZ**; (c) Photos of **2GCzBPPZ** at various temperatures (UV torch λ_{exc} = 360 nm); (d)

Ratiometric plot of I_{575}/I_{475} vs temperature upon decreasing the temperature below RT; (e) Ratiometric plot of I_{475}/I_{575} vs temperature upon increasing the temperature from RT (right); (f) Schematic representation of the thermal response and two-state equilibration model describing the observed abnormal temperature-responsive dual emission phenomenon of **2GCzBPPZ**. (g) Spatio-temperature sensor application in paraffin wax (paraffin embedded with **2GCzBPPZ** in a test tube (length:160 mm, diameter: 16 mm) excited with a UV torch, λ_{exc}= 360 nm).

TADF properties in the solid state

To assess the emission properties of **2GCzBPPZ** and **2GCzBPN** in the solid state, their photophysical properties were investigated in an OLED-relevant host 1,3-bis(*N*-carbazolyl)benzene (mCP) as this host matrix has a sufficiently high triplet energy (T_1 = 2.91 eV)[76] to confine the excitons onto the emitter. As shown in Figure **6**, as 10 wt% doped films in mCP, **2GCzBPN** emits at λ_{PL} of 601 nm, which is red-shifted compared to **2GCzBPPZ**, which emits at λ_{PL} of 531 nm (Table **1**). The corresponding photoluminescence quantum yield (Φ_{PL}) of **2GCzBPN** and **2GCzBPPZ** are 71 and 57%, respectively, which decrease to 60 and 45%, respectively, under air. The S_1/T_1 energy levels of **2GCzBPPZ** (2.76/2.50 eV) and **2GCzBPN** (2.38/2.26 eV) were inferred from the onsets of the prompt fluorescence and phosphorescence spectra, respectively, at 77 K (Figure **7a** and **b**). For **2GCzBPN**, both the fluorescence and phosphorescence spectra are broad and structureless, indicating that both the S_1 and T_1 states have CT character. However, the phosphorescence spectrum of **2GCzBPPZ** is structured, suggesting that the T_1 state has LE character, while the S_1 state is CT in character. The corresponding ΔE_{ST} values are 0.26 and 0.12 eV for **2GCzBPPZ** and **2GCzBPN**, respectively, which matched the trend observed in 2-MeTHF glass at 77 K (ΔE_{ST} of 0.17 eV for **2GCzBPPZ** and 0.14 eV for **2GCzBPN**). The room temperature emission from both compounds shows multiexponential decay kinetics, with average prompt fluorescence lifetimes, τ_p, of 18.0 and 34.1 ns, and average delayed emission lifetimes, τ_d, of 73.1 and 2.9 μs for **2GCzBPPZ** and **2GCzBPN**, respectively (Figure **7d**). The corresponding rate constants of intersystem crossing (k_{ISC}) for both compounds in mCP films are 1.61×10^7 s^{-1} and 0.45×10^7 s^{-1} for **2GCzBPPZ,** and **2GCzBPN**, respectively, while the rate constants of reverse intersystem crossing (k_{RISC}) for **2GCzBPN** reached 4.1×10^5 s^{-1}, a value 20 times faster than in **2GCzBPPZ** of 1.93×10^4 s^{-1}. The relative intensities of the delayed PL increased with increasing temperature from 100 K to 298 K, corroborating the TADF nature of the emission of both compounds in the mCP films (Figure **7e** and **f**).

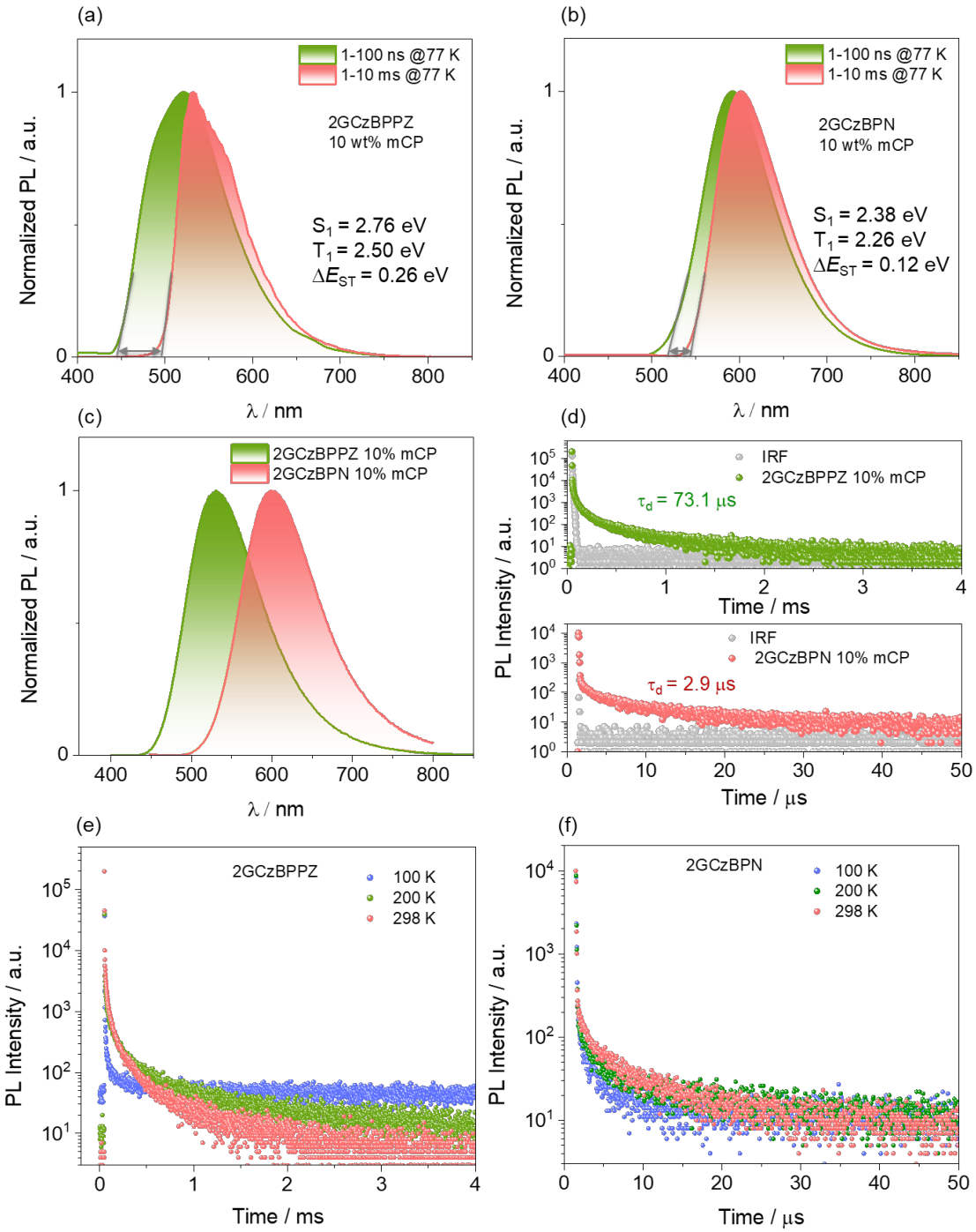

Figure 7. Prompt fluorescence (1-100 ns) and phosphorescence spectra (1-10 ms) in 10 wt% doped in mCP at 77 K of (a) **2GCzBPPZ** and (b) **2GCzBPN** (λ_{exc} = 345 nm). (c) Steady-state PL spectra of 10 wt% doped films of **2GCzBPPZ** and **2GCzBPN** in mCP film at room temperature (λ_{exc} =345 nm); (d) PL decay of 10 wt% doped films of **2GCzBPPZ** and **2GCzBPN** in mCP at 298 K (λ_{exc} =375 nm); Temperature-dependent PL decay of 10 wt% doped films of (e) **2GCzBPPZ** and (f) **2GCzBPN** in mCP (λ_{exc}= 375 nm).

Table **1**. Photophysical properties of **2GCzBPPZ** and **2GCzBPN**.

	λ_{abs}/(ε / $\times10^3$ M^{-1} cm^{-1})[a] / nm	λ_{PL}[a] / nm	S_1/T_1[b] / eV	ΔE_{ST}[b] / eV	λ_{PL}[c] / nm	Φ_{PL}[c] / %	τ_p[d] / ns	τ_d[d] / μs	S_1/T_1[e] / eV	ΔE_{ST}[e] / eV	HOMO[f] / eV	LUMO[f] / eV	ΔE[f] / eV
2GCzBPPZ	346 (45), 400(19), 432(19)	534	2.63/2.46	0.17	531	57 (45)	18.0	73.1	2.71/ 2.50	0.26	-5.30	-2.94	2.36
2GCzBPN	348 (51), 397(15), 475(10)	624	2.35/2.21	0.14	601	71 (60)	34.1	2.9	2.38/ 2.26	0.12	-5.22	-3.21	2.01

[a] In PhMe at 298 K (λ_{exc} = 340 nm). [b] Obtained from the onset of the prompt fluorescence (time window: 1 ns – 100 ns) and phosphorescence spectra (time window: 1 ms – 10 ms) measured in 2-MeTHF glass at 77 K, λ_{exc} = 343 nm. [c] Thin films of 10 wt% emitters doped in mCP were prepared by spin-coating, and Φ_{PL} values were determined using an integrating sphere (λ_{exc} = 345 nm). Values quoted are under N_2. Values in parentheses are in air. [d]Average lifetime ($\tau_{avg} = \Sigma A_i\tau_i^2 / \Sigma A_i\tau_i$, where A_i is the pre-exponential for lifetime τ_i). Prompt and delayed emissions were measured by TCSPC and MCS, respectively (λ_{exc} = 379 nm). [e] S_1 was obtained from the onset of the prompt emission (time window: 1–100 ns) measured in doped film at 77 K and T_1 was obtained from the onset of the phosphorescence spectrum (time window: 1–10 ms) measured in doped film at 77 K. [f] In DCM with 0.1 M [^{n}Bu$_4$N]PF$_6$ as the supporting electrolyte and Fc/Fc^+ as the internal reference (0.46 V vs. SCE).[66] The HOMO and LUMO energies were determined using $E_{HOMO/LUMO}$= - (E_{ox}/ E_{red} +4.8) eV where E_{ox} and E_{red} are anodic and cathodic peak potentials versus Fc/Fc^+, respectively, obtained from the DPV.[66] [g] $\Delta E = |E_{HOMO}-E_{LUMO}|$.

OLED characterization

We next fabricated solution-processed (SP) OLEDs employing 10 wt% emitters doped in mCP films as the emissive layer (EML) using the following device stack: ITO (indium tin oxide)/ poly(3,4-ethylenedioxythiophene):poly(styrenesulfonate) (PEDOT:PSS) (40 nm)/ mCP (60%): oxadiazolyl]phenylene (OXD-7) (30%): 10 wt% emitters (20 nm)/ (3,3′-(5′-(3-(pyridin-3-yl)phenyl)-[1,1′:3′,1″-terphenyl]-3,3″-diyl)dipyridine) (TmPyPB) (45 nm)/LiF (1 nm)/Al (Figure **8a** and **b**), where ITO and Al serve as the anode and cathode, respectively, and PEDOT:PSS and TmPyPB are the hole-transporting layer electron-transporting layer, respectively. As shown in Figure **8b**, the OLEDs with **2GCzBPPZ** and **2GCzBPN** exhibit green and orange emission with emission maxima, λ_{EL}, of 552 and 608 nm and corresponding Commission Internationale de L'Éclairage (CIE) coordinates of (0.39, 0.55) and (0.58, 0.40), respectively, which match the PL emission (Figure **8c**). The devices with **2GCzBPPZ** showed lower turn-on voltages (V_{on}) of 3.5 V and high brightness of up to 8000 cd m^{-2} compared to V_{on} of 4.1 V and a maximum luminance of 1068 cd m^{-2} for the devices with **2GCzBPN** (Figure

8c and Table **2**). At the same voltages, the current density (*J*) of the **2GCzBPN**-based device is lower than that of the **2GCzBPPZ**-based device, which we ascribe to the relatively lower electron mobility of **2GCzBPN** in the mCP film. The devices with **2GCzBPPZ** showed a higher maximum external quantum efficiency (EQE_{max}) of 15.0% at 581 cd m^{-2} with negligible efficiency roll-off at 1000 cd m^{-2} (EQE_{1000} = 14.0%), while the devices with **2GCzBPN** showed poorer performance, with EQE_{max} of 5.3% (Figure **8d**). Considering the measured Φ_{PL} (Table **1**) and assuming 25% outcoupling efficiency associated with an isotropic orientation of the transition dipole moment of the emitter, the EQE_{max} for devices with **2GCzBPPZ** and **2GCzBPN** were expected to be 14.3% and 17.8%, respectively. This indicates that the device with **2GCzBPPZ** has effectively unity exciton utilization efficiency, which that can be attributed to the stabilizing effect of aggregation on excitons;[77] however, at this stage it is unclear why the EQE_{max} for **2GCzBPN** is so low.

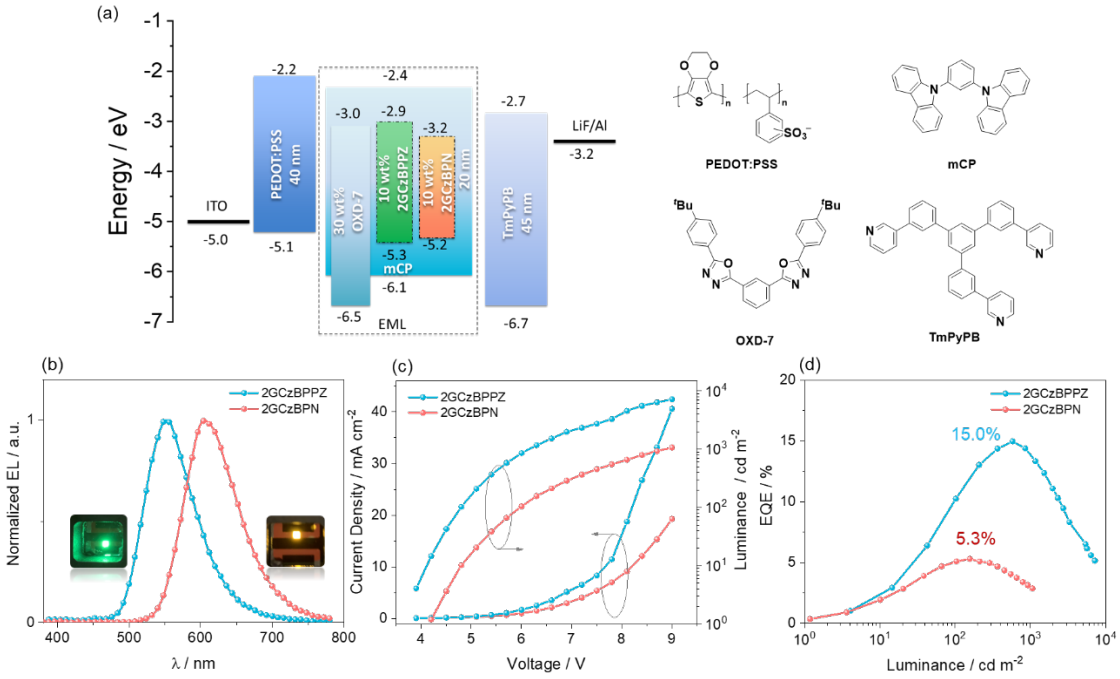

Figure **8**. (a) Energy level diagram and structure of materials used in the devices; (b) EL spectra, (c) Current density and luminance versus voltage characteristics, (d) External quantum efficiency versus luminance curves for the devices.

Table **2**. Electroluminescence data for the devices

Emitter	V_{on} [a] / V	λ_{EL} [b] / nm	L_{max}/ cd m^{-2}	CE / cd A^{-1}	PE_{max} / lm W^{-1}	EQE[c] / %	CIE[d] / x,y
2GCzBPPZ	3.5	552	7207	51.7	28.8	15.0/10.2/14.0	0.39, 0.55
2GCzBPN	4.1	608	1068	10.2	5.1	5.3/5.1/3.0	0.58, 0.40

[a] The turn-on voltage at a brightness ≈ 1 cd m^{-2}. [b] The electroluminescence maximum recorded at 6 V. [c] EQE_{max}/EQE_{100}/ EQE_{1000}. [d] The CIE coordinates recorded at 6 V

Conclusions

Here, we designed two TADF dendrimers **2GCzBPPZ** and **2GCzBPN** by using different rigid and planar nitrogen-doped PAHs as the acceptors combined with two second-generation tercarbazole donor dendrons. Due to less twisted geometry adopted and the use of the large π-conjugation acceptor, **2GCzBPPZ** shows an unusual white emission in *n*-hexane solution that results from dual emission from a combination of monomer and aggregates emitting, respectively, at 475 nm and 575 nm. The dual emission behavior of **2GCzBPPZ** is quite sensitive to both the concentration and temperature. We exploited this dual emission behavior in a temperature sensor by embedding **2GCzBPPZ** in paraffin. To the best of our knowledge, **2GCzBPPZ** shows the broadest spectra and temperature response of any organic temperature sensor. Due to its more twisted geometry, **2GCzBPN** shows efficient TADF and there is neither significant aggregate formation nor dual emission. Finally, we employed these two compounds as emitters in solution-processed OLEDs. The SP-OLEDs with **2GCzBPPZ** showed around a three-times higher EQE_{max} of 15.0% at λ_{EL} of 552 nm than the device with **2GCzBPN** (EQE_{max} = 5.3% at λ_{EL}= 608 nm). We are currently investigating the origin for this divergence in performance.

Acknowledgments

Changfeng Si thanks the China Scholarship Council (201806890001). D.S acknowledges support from the Royal Academy of Engineering Enterprise Fellowship (EF2122-13106). We thank the Engineering and Physical Sciences Research Council for support (EP/R035164/1; EP/W007517). We thank Dr. Tao Wang, Dr. Biju Basumatary and Prof. A.P. de Silva for helpful discussions.

Conflict of Interest

The authors have filed a patent application GB2315830.6 covering this material and its use as a temperature sensor and emitter for OLEDs.

Supporting Information

^{1}H and ^{13}C NMR spectra, HRMS, EA and HPLC of all target compounds; supplementary computational data; supplementary photophysical data.

References

(1) Sun, D.; Si, C.; Wang, T.; Zysman-Colman, E. 1,3,5-Triazine-Functionalized Thermally Activated Delayed Fluorescence Emitters for Organic Light-Emitting Diodes. *Adv. Photonics Res.* **2022**, 2200203. https://doi.org/10.1002/adpr.202200203.

(2) Wong, M. Y.; Zysman-Colman, E. Purely Organic Thermally Activated Delayed Fluorescence Materials for Organic Light-Emitting Diodes. *Adv. Mater.* **2017**, *29* (22), 1605444. https://doi.org/10.1002/adma.201605444.

(3) Uoyama, H.; Goushi, K.; Shizu, K.; Nomura, H.; Adachi, C. Highly Efficient Organic Light-Emitting Diodes from Delayed Fluorescence. *Nature* **2012**, *492* (7428), 234–238. https://doi.org/10.1038/nature11687.

(4) Etherington, M. K.; Gibson, J.; Higginbotham, H. F.; Penfold, T. J.; Monkman, A. P. Revealing the Spin-Vibronic Coupling Mechanism of Thermally Activated Delayed Fluorescence. *Nat. Commun.* **2016**, *7* (1), 13680. https://doi.org/10.1038/ncomms13680.

(5) Qian, H.; Cousins, M. E.; Horak, E. H.; Wakefield, A.; Liptak, M. D.; Aprahamian, I. Suppression of Kasha's Rule as a Mechanism for Fluorescent Molecular Rotors and Aggregation-Induced Emission. *Nat. Chem.* **2017**, *9* (1), 83–87. https://doi.org/10.1038/nchem.2612.

(6) Demchenko, A. P.; Tomin, V. I.; Chou, P. T. Breaking the Kasha Rule for More Efficient Photochemistry. *Chem. Rev.* **2017**, *117* (21), 13353–13381. https://doi.org/10.1021/acs.chemrev.7b00110.

(7) Liu, Y.; Xie, G.; Ren, Z.; Yan, S. Thermally Activated Delayed Fluorescence Polymer Emitters with Tunable Emission from Yellow to Warm White Regulated by Triphenylamine Derivatives. *ACS Appl. Polym. Mater.* **2019**, *1* (8), 2204–2212. https://doi.org/10.1021/acsapm.9b00461.

(8) Christopherson, C. J.; Mayder, D. M.; Poisson, J.; Paisley, N. R.; Tonge, C. M.; Hudson, Z. M. 1,8-Naphthalimide-Based Polymers Exhibiting Deep-Red Thermally Activated Delayed Fluorescence and Their Application in Ratiometric Temperature Sensing. *ACS Appl. Mater. Interfaces* **2020**, *12* (17), 20000–20011. https://doi.org/10.1021/acsami.0c05257.

(9) Luo, M.; Li, X.; Ding, L.; Baryshnikov, G.; Shen, S.; Zhu, M.; Zhou, L.; Zhang, M.; Lu, J.; Ågren, H.; Wang, X.; Zhu, L. Integrating Time-Resolved Imaging Information by Single-Luminophore Dual Thermally Activated Delayed Fluorescence. *Angew. Chemie* **2020**, *132* (39), 17166–17173. https://doi.org/10.1002/ange.202009077.

(10) Tanaka, H.; Shizu, K.; Nakanotani, H.; Adachi, C. Dual Intramolecular Charge-Transfer Fluorescence Derived from a Phenothiazine-Triphenyltriazine Derivative. *J. Phys. Chem. C* **2014**, *118* (29), 15985–15994. https://doi.org/10.1021/jp501017f.

(11) Cai, X.; Qiao, Z.; Li, M.; Wu, X.; He, Y.; Jiang, X.; Cao, Y.; Su, S. J. Purely Organic Crystals Exhibit Bright Thermally Activated Delayed Fluorescence. *Angew. Chemie - Int. Ed.* **2019**, *58* (38), 13522–13531. https://doi.org/10.1002/anie.201906371.

(12) Li, X.; Baryshnikov, G.; Deng, C.; Bao, X.; Wu, B.; Zhou, Y.; Ågren, H.; Zhu, L. A Three-Dimensional Ratiometric Sensing Strategy on Unimolecular Fluorescence–Thermally Activated Delayed Fluorescence Dual Emission. *Nat. Commun.* **2019**, *10* (1), 1–9. https://doi.org/10.1038/s41467-019-08684-2.

(13) Geng, Y.; D'Aleo, A.; Inada, K.; Cui, L.; Kim, J. U.; Nakanotani, H.; Adachi, C. Donor–σ–Acceptor Motifs: Thermally Activated Delayed Fluorescence Emitters with Dual Upconversion. *Angew. Chemie* **2017**, *129* (52), 16763–16767. https://doi.org/10.1002/ange.201708876.

(14) Xie, Z.; Huang, Q.; Yu, T.; Wang, L.; Mao, Z.; Li, W.; Yang, Z.; Zhang, Y.; Liu, S.; Xu, J.; Chi, Z.; Aldred, M. P. Hydrogen-Bonding-Assisted Intermolecular Charge Transfer: A New Strategy to Design Single-Component White-Light-Emitting Materials. *Adv. Funct. Mater.* **2017**, *27* (47). https://doi.org/10.1002/adfm.201703918.

(15) Chen, J.; Yu, T.; Ubba, E.; Xie, Z.; Yang, Z.; Zhang, Y.; Liu, S.; Xu, J.; Aldred, M. P.; Chi, Z. Achieving Dual-Emissive and Time-Dependent Evolutive Organic Afterglow by Bridging Molecules with Weak Intermolecular Hydrogen Bonding. *Adv. Opt. Mater.* **2019**, *7* (7), 1801593. https://doi.org/10.1002/adom.201801593.

(16) Zhang, X.; Lu, T.; Zhou, C.; Liu, H.; Wen, Y.; Shen, Y.; Li, B.; Zhang, S. T.; Yang, B. Thermally Activated Delayed Fluorescence of Aggregates Induced by Strong π-π Interactions and Reversible Dual-Responsive Luminescence Switching. *CCS Chem.* **2022**, *4* (2), 625–637. https://doi.org/10.31635/ccschem.021.202000731.

(17) Chen, X.; He, Z.; Kausar, F.; Chen, G.; Zhang, Y.; Yuan, W. Z. Aggregation-Induced Dual Emission and Unusual Luminescence beyond Excimer Emission of Poly(Ethylene Terephthalate). *Macromolecules* **2018**, *51* (21), 9035–9042. https://doi.org/10.1021/acs.macromol.8b01743.

(18) Feng, X.; Qi, C.; Feng, H. T.; Zhao, Z.; Sung, H. H. Y.; Williams, I. D.; Kwok, R. T. K.; Lam, J. W. Y.; Qin, A.; Tang, B. Z. Dual Fluorescence of Tetraphenylethylene-Substituted Pyrenes with Aggregation-Induced Emission Characteristics for White-Light Emission. *Chem. Sci.* **2018**, *9* (25), 5679–5687. https://doi.org/10.1039/c8sc01709c.

(19) Liu, Y.; Nishiura, M.; Wang, Y.; Hou, Z. π-Conjugated Aromatic Enynes as a Single-Emitting Component for White Electroluminescence. *J. Am. Chem. Soc.* **2006**, *128* (17), 5592–5593. https://doi.org/10.1021/ja058188f.

(20) Filby, M. H.; Dickson, S. J.; Zaccheroni, N.; Prodi, L.; Bonacchi, S.; Montalti, M.; Paterson, M. J.; Humphries, T. D.; Chiorboli, C.; Steed, J. W. Induced Fit Interanion Discrimination by Binding-Induced Excimer Formation. *J. Am. Chem. Soc.* **2008**, *130* (12), 4105–4113. https://doi.org/10.1021/ja711012d.

(21) Yang, Q. Y.; Lehn, J. M. Bright White-Light Emission from a Single Organic Compound in the Solid State. *Angew. Chemie - Int. Ed.* **2014**, *53* (18), 4572–4577. https://doi.org/10.1002/anie.201400155.

(22) Yoshii, R.; Hirose, A.; Tanaka, K.; Chujo, Y. Functionalization of Boron Diiminates with Unique Optical Properties: Multicolor Tuning of Crystallization-Induced Emission and Introduction into the Main Chain of Conjugated Polymers. *J. Am. Chem. Soc.* **2014**, *136* (52), 18131–18139. https://doi.org/10.1021/ja510985v.

(23) Neelakandan, P. P.; Ramaiah, D. DNA-Assisted Long-Lived Excimer Formation in a Cyclophane. *Angew. Chemie - Int. Ed.* **2008**, *47* (44), 8407–8411. https://doi.org/10.1002/anie.200803162.

(24) Mansell, D.; Rattray, N.; Etchells, L. L.; Schwalbe, C. H.; Blake, A. J.; Bichenkova, E. V.; Bryce, R. A.; Barker, C. J.; Díaz, A.; Kremer, C.; Freeman, S. Fluorescent Probe: Complexation of Fe3+with the Myo-Inositol 1,2,3-Trisphosphate Motif. *Chem. Commun.* **2008**, No. 41, 5161. https://doi.org/10.1039/b809238a.

(25) Thirion, D.; Romain, M.; Rault-Berthelot, J.; Poriel, C. Intramolecular Excimer Emission as a Blue Light Source in Fluorescent Organic Light Emitting Diodes: A Promising Molecular Design. *J. Mater. Chem.* **2012**, *22* (15), 7149–7157. https://doi.org/10.1039/c2jm16774c.

(26) Shih, P. I.; Chuang, C. Y.; Chien, C. H.; Diau, E. W. G.; Shu, C. F. Highly Efficient Non-Doped Blue-Light-Emitting Diodes Based on an Anthrancene Derivative End-Capped with Tetraphenylethylene Groups. *Adv. Funct. Mater.* **2007**, *17* (16), 3141–3146. https://doi.org/10.1002/adfm.200700355.

(27) Klärner, G.; Davey, M. H.; Chen, W.-D.; Scott, J. C.; Miller, R. D. Colorfast Blue-Light-Emitting Random Copolymers Derived from Di-n-Hexylfluorene and Anthracene. *Adv. Mater.* **1998**, *10* (13), 993–997. https://doi.org/10.1002/(SICI)1521-4095(199809)10:13<993::AID-ADMA993>3.0.CO;2-2.

(28) Zhang, J.; Zhao, X.; Shen, H.; Lam, J. W. Y.; Zhang, H.; Tang, B. Z. White-Light Emission from Organic Aggregates: A Review. *Adv. Photonics* **2021**, *4*, 014001. https://doi.org/10.1117/1.AP.4.1.014001.

(29) Tan, J. H.; Chen, W. C.; Ni, S. F.; Qiu, Z.; Zhan, Y.; Yang, Z.; Xiong, J.; Cao, C.; Huo, Y.; Lee, C. S. Aggregation-State Engineering and Emission Switching in D-A-D′ AIEgens Featuring Dual Emission, MCL and White Electroluminescence. *J. Mater. Chem. C* **2020**, *8* (24), 8061–8068. https://doi.org/10.1039/d0tc01733g.

(30) Teng, M. J.; Jia, X. R.; Yang, S.; Chen, X. F.; Wei, Y. Reversible Tuning Luminescent Color and Emission Intensity: A Dipeptide-Based Light-Emitting Material. *Adv. Mater.* **2012**, *24* (9), 1255–1261. https://doi.org/10.1002/adma.201104592.

(31) Zhang, Q.; Mao, Q.; Shang, C.; Chen, Y. N.; Peng, X.; Tan, H.; Wang, H. Simple Aliphatic Oximes as Nonconventional Luminogens with Aggregation-Induced Emission Characteristics. *J. Mater. Chem. C* **2017**, *5* (15), 3699–3705. https://doi.org/10.1039/c7tc00783c.

(32) Spano, F. C. The Spectral Signatures of Frenkel Polarons in H- And J-Aggregates. *Acc. Chem. Res.* **2010**, *43* (3), 429–439. https://doi.org/10.1021/ar900233v.

(33) Ma, S.; Du, S.; Pan, G.; Dai, S.; Xu, B.; Tian, W. Organic Molecular Aggregates: From Aggregation Structure to Emission Property. *Aggregate* **2021**, *2*, e96. https://doi.org/10.1002/agt2.96.

(34) Dimitriev, O. P.; Piryatinski, Y. P.; Slominskii, Y. L. Excimer Emission in J-Aggregates. *J. Phys. Chem. Lett.* **2018**, *9* (9), 2138–2143. https://doi.org/10.1021/acs.jpclett.8b00481.

(35) Zhao, C.; Ding, Z.; Zhang, Y.; Ni, Z.; Li, S.; Gong, S.; Zou, B.; Wang, K.; Yu, L. Thermally Activated Delayed Fluorescence with Dual-Emission and Pressure-Induced Bidirectional Shifting: Cooperative Effects of Intramolecular and Intermolecular Energy Transfer. *Chem. Sci.* **2023**, *14* (5), 1089–1096. https://doi.org/10.1039/d2sc05792a.

(36) Qin, T.; Liu, B.; Zhu, K.; Luo, Z.; Huang, Y.; Pan, C.; Wang, L. Organic Fluorescent Thermometers: Highlights from 2013 to 2017. *TrAC - Trends Anal. Chem.* **2018**, *102*, 259–271. https://doi.org/10.1016/j.trac.2018.03.003.

(37) Sun, Y.; Fu, M.; Bian, M.; Zhu, Q. Recent Progress on Small Molecular Temperature-Sensitive Fluorescent Probes. *Biotechnol. Bioeng.* **2023**, *120* (1), 7–21. https://doi.org/10.1002/bit.28250.

(38) Mazza, M. M. A.; Raymo, F. M. Structural Designs for Ratiometric Temperature Sensing with Organic Fluorophores. *J. Mater. Chem. C* **2019**, *7* (18), 5333–5342. https://doi.org/10.1039/C9TC00993K.

(39) Vetrone, F.; Naccache, R.; Zamarrón, A.; Juarranz de la Fuente, A.; Sanz-Rodríguez, F.; Martinez Maestro, L.; Martín Rodriguez, E.; Jaque, D.; García Solé, J.; Capobianco, J. A. Temperature Sensing Using Fluorescent Nanothermometers. *ACS Nano* **2010**, *4* (6), 3254–3258. https://doi.org/10.1021/nn100244a.

(40) Feng, G.; Zhang, H.; Zhu, X.; Zhang, J.; Fang, J. Fluorescence Thermometers: Intermediation of Fundamental Temperature and Light. *Biomater. Sci.* **2022**, *10* (8), 1855–1882. https://doi.org/10.1039/D1BM01912K.

(41) Ogle, M. M.; Smith McWilliams, A. D.; Jiang, B.; Martí, A. A. Latest Trends in Temperature Sensing by Molecular Probes. *ChemPhotoChem* **2020**, *4* (4), 255–270. https://doi.org/10.1002/cptc.201900255.

(42) Pfeiffer, S. A.; Nagl, S. Microfluidic Platforms Employing Integrated Fluorescent or Luminescent Chemical Sensors: A Review of Methods, Scope and Applications. *Methods Appl. Fluoresc.* **2015**, *3* (3), 034003. https://doi.org/10.1088/2050-6120/3/3/034003.

(43) Pais, V. F.; Lassaletta, J. M.; Fernández, R.; El-Sheshtawy, H. S.; Ros, A.; Pischel, U. Organic Fluorescent Thermometers Based on Borylated Arylisoquinoline Dyes. *Chem. - A Eur. J.* **2014**, *20* (25), 7638–7645. https://doi.org/10.1002/chem.201402027.

(44) Uchiyama, S.; Gota, C. Luminescent Molecular Thermometers for the Ratiometric Sensing of Intracellular Temperature. *Rev. Anal. Chem.* **2017**, *36* (1), 20160021. https://doi.org/10.1515/revac-2016-0021.

(45) Feng, J.; Xiong, L.; Wang, S.; Li, S.; Li, Y.; Yang, G. Fluorescent Temperature Sensing Using Triarylboron Compounds and Microcapsules for Detection of a Wide Temperature Range on the Micro- and Macroscale. *Adv. Funct. Mater.* **2013**, *23* (3), 340–345. https://doi.org/10.1002/adfm.201201712.

(46) Jenkins, J.; Borisov, S. M.; Papkovsky, D. B.; Dmitriev, R. I. Sulforhodamine Nanothermometer for Multiparametric Fluorescence Lifetime Imaging Microscopy. *Anal. Chem.* **2016**, *88* (21), 10566–10572. https://doi.org/10.1021/acs.analchem.6b02675.

(47) Feng, J.; Tian, K.; Hu, D.; Wang, S.; Li, S.; Zeng, Y.; Li, Y.; Yang, G. A Triarylboron-Based Fluorescent Thermometer: Sensitive over a Wide Temperature Range. *Angew. Chemie - Int. Ed.* **2011**, *50* (35), 8072–8076. https://doi.org/10.1002/anie.201102390.

(48) Ito, A.; Ishizaka, S.; Kitamura, N. A Ratiometric TICT-Type Dual Fluorescent Sensor for an Amino Acid. *Phys. Chem. Chem. Phys.* **2010**, *12* (25), 6641–6649. https://doi.org/10.1039/b924176k.

(49) Meng, L.; Jiang, S.; Song, M.; Yan, F.; Zhang, W.; Xu, B.; Tian, W. TICT-Based Near-Infrared Ratiometric Organic Fluorescent Thermometer for Intracellular Temperature Sensing. *ACS Appl. Mater. Interfaces* **2020**, *12* (24), 26842–26851. https://doi.org/10.1021/acsami.0c03714.

(50) Baleizão, C.; Berberan-Santos, M. N. Thermally Activated Delayed Fluorescence in Fullerenes. *Ann. N. Y. Acad. Sci.* **2008**, *1130*, 224–234. https://doi.org/10.1196/annals.1430.044.

(51) Steinegger, A.; Klimant, I.; Borisov, S. M. Purely Organic Dyes with Thermally Activated Delayed Fluorescence—A Versatile Class of Indicators for Optical Temperature Sensing. *Adv. Opt. Mater.* **2017**, *5* (18), 1700372. https://doi.org/10.1002/adom.201700372.

(52) Paisley, N. R.; Tonge, C. M.; Hudson, Z. M. Stimuli-Responsive Thermally Activated Delayed Fluorescence in Polymer Nanoparticles and Thin Films: Applications in Chemical Sensing and Imaging. *Front. Chem.* **2020**, *8*, 229. https://doi.org/10.3389/fchem.2020.00229.

(53) Fang, F.; Zhu, L.; Li, M.; Song, Y.; Sun, M.; Zhao, D.; Zhang, J. Thermally Activated Delayed Fluorescence Material: An Emerging Class of Metal-Free Luminophores for Biomedical Applications. *Adv. Sci.* **2021**, *8* (24), 2102970. https://doi.org/10.1002/advs.202102970.

(54) Augusto, V.; Baleizão, C.; Berberan-Santos, M. N.; Farinha, J. P. S. Oxygen-Proof Fluorescence Temperature Sensing with Pristine C70 Encapsulated in Polymer Nanoparticles. *J. Mater. Chem.* **2010**, *20* (6), 1192–1197. https://doi.org/10.1039/b920673f.

(55) Baleizão, C.; Nagl, S.; Borisov, S. M.; Schäferling, M.; Wolfbeis, O. S.; Berberan-Santos, M. N. An Optical Thermometer Based on the Delayed Fluorescence of C70. *Chem. - A Eur. J.* **2007**, *13* (13), 3643–3651. https://doi.org/10.1002/chem.200601580.

(56) Fister, J. C.; Rank, D.; Harris, J. M. Delayed Fluorescence Optical Thermometry. *Anal. Chem.* **1995**, *67* (23), 4269–4275. https://doi.org/10.1021/ac00119a011.

(57) Adamo, C.; Barone, V. Toward Reliable Density Functional Methods without Adjustable Parameters: The PBE0 Model. *J. Chem. Phys.* **1999**, *110* (13), 6158–6170. https://doi.org/10.1063/1.478522.

(58) Petersson, G. A.; Tensfeldt, T. G.; Montgomery, J. A. A Complete Basis Set Model Chemistry. III. The Complete Basis Set-Quadratic Configuration Interaction Family of Methods. *J. Chem. Phys.* **1991**, *94* (9), 6091–6101. https://doi.org/10.1063/1.460448.

(59) Kerwin, S. M. ChemBioOffice Ultra 2010 Suite. *J. Am. Chem. Soc.* **2010**, *132* (7), 2466–2467. https://doi.org/10.1021/ja1005306.

(60) *At the S1 Geometries, for BPNBP2GCz, S1=2.16 EV, T1=2.11 EV, Totally CT for S1 and T1; for 2GCzBPN, S1=1.50 EV, T1=1.48 EV, Totally CT for Both.*

(61) Hirata, S.; Head-Gordon, M. Time-Dependent Density Functional Theory within the Tamm-Dancoff Approximation. *Chem. Phys. Lett.* **1999**, *314* (3–4), 291–299. https://doi.org/10.1016/S0009-2614(99)01149-5.

(62) Grimme, S. Density Functional Calculations with Configuration Interaction for the Excited States of Molecules. *Chem. Phys. Lett.* **1996**, *259* (1–2), 128–137. https://doi.org/10.1016/0009-2614(96)00722-1.

(63) Humphrey, W.; Dalke, A.; Schulten, K. VMD: Visual Molecular Dynamics. *J. Mol. Graph.* **1996**, *14* (1), 33–38. https://doi.org/10.1016/0263-7855(96)00018-5.

(64) Duda, E.; Hall, D.; Bagnich, S.; Carpenter-Warren, C. L.; Saxena, R.; Wong, M. Y.; Cordes, D. B.; Slawin, A. M. Z.; Beljonne, D.; Olivier, Y.; Zysman-Colman, E.; Köhler, A. Enhancing Thermally Activated Delayed Fluorescence by Fine-Tuning the Dendron Donor Strength. *J. Phys. Chem. B* **2022**, *126* (2), 552–562. https://doi.org/10.1021/acs.jpcb.1c05749.

(65) Sun, D.; Duda, E.; Fan, X.; Saxena, R.; Zhang, M.; Bagnich, S.; Zhang, X.; Köhler, A.; Zysman-Colman, E. Thermally Activated Delayed Fluorescent Dendrimers That Underpin High-Efficiency Host-Free Solution-Processed Organic Light-Emitting Diodes. *Adv. Mater.* **2022**, *34* (23), 2110344. https://doi.org/10.1002/adma.202110344.

(66) Connelly, N. G.; Geiger, W. E. Chemical Redox Agents for Organometallic Chemistry. *Chem. Rev.* **1996**, *96* (2), 877–910. https://doi.org/10.1021/cr940053x.

(67) Sun, D.; Saxena, R.; Fan, X.; Athanasopoulos, S.; Duda, E.; Zhang, M.; Bagnich, S.; Zhang, X.; Zysman-Colman, E.; Köhler, A. Regiochemistry of Donor Dendrons Controls the Performance of Thermally Activated Delayed Fluorescence Dendrimer Emitters for High Efficiency Solution-Processed Organic Light-Emitting Diodes. *Adv. Sci.* **2022**, *9* (20), 2201470. https://doi.org/10.1002/advs.202201470.

(68) Furue, R.; Matsuo, K.; Ashikari, Y.; Ooka, H.; Amanokura, N.; Yasuda, T. Highly Efficient Red–Orange Delayed Fluorescence Emitters Based on Strong π-Accepting Dibenzophenazine and Dibenzoquinoxaline Cores: Toward a Rational Pure-Red OLED Design. *Adv. Opt. Mater.* **2018**, *6* (5), 1701147. https://doi.org/10.1002/adom.201701147.

(69) Förster, T. Excimers. *Angew. Chemie Int. Ed. English* **1969**, *8* (5), 333–343. https://doi.org/10.1002/anie.196903331.

(70) Chen, Z.; Fimmel, B.; Würthner, F. Solvent and Substituent Effects on Aggregation Constants of Perylene Bisimide π-Stacks - A Linear Free Energy Relationship

Analysis. *Org. Biomol. Chem.* **2012**, *10* (30), 5845–5855. https://doi.org/10.1039/c2ob07131b.

(71) Simionesie, D.; O'Callaghan, G.; Manning, J. R. H.; Düren, T.; Preece, J. A.; Evans, R.; Zhang, Z. J. Combined Experimental and Computational Study of Polycyclic Aromatic Compound Aggregation: The Impact of Solvent Composition. *Polycycl. Aromat. Compd.* **2022**, *0* (0), 1–20. https://doi.org/10.1080/10406638.2022.2077777.

(72) Yang, J.; Fang, M.; Li, Z. Organic Luminescent Materials: The Concentration on Aggregates from Aggregation-induced Emission. *Aggregate* **2020**, *1* (1), 6–18. https://doi.org/10.1002/agt2.2.

(73) Peng, Q.; Yang, L.; Li, Y.; Zhang, Y.; Li, T.; Qin, Y.; Song, Y.; Hou, H.; Li, K. Aggregation/Viscosity-Induced Emission and Third-Order Nonlinear Optical Signal Inversion in a TICT System. *J. Phys. Chem. C* **2020**, *124* (41), 22684–22691. https://doi.org/10.1021/acs.jpcc.0c06533.

(74) Hong, Y.; Lam, J. W. Y. Y.; Tang, B. Z. Aggregation-Induced Emission: Phenomenon, Mechanism and Applications. *Chem. Commun.* **2009**, No. 29, 4332–4353. https://doi.org/10.1039/b904665h.

(75) Ruan, H.; Zhang, Y.; Wang, Q.; Wang, C.; Wang, T. A Novel Earthworm-Inspired Smart Lubrication Material with Self-Healing Function. *Tribol. Int.* **2022**, *165*, 107303. https://doi.org/10.1016/j.triboint.2021.107303.

(76) Zeng, W.; Zhou, T.; Ning, W.; Zhong, C.; He, J.; Gong, S.; Xie, G.; Yang, C. Realizing 22.5% External Quantum Efficiency for Solution-Processed Thermally Activated Delayed-Fluorescence OLEDs with Red Emission at 622 nm via a Synergistic Strategy of Molecular Engineering and Host Selection. *Adv. Mater.* **2019**, *31* (33), 1901404. https://doi.org/10.1002/adma.201901404.

(77) Liu, D.; Zhang, M.; Tian, W.; Jiang, W.; Sun, Y.; Zhao, Z.; Tang, B. Z. Molecular Core–Shell Structure Design: Facilitating Delayed Fluorescence in Aggregates toward Highly Efficient Solution-processed OLEDs. *Aggregate* **2022**, *3*, e163. https://doi.org/10.1002/agt2.164.

TOC Graphic